Analysis, Design, and Implementation of Impulse-Injection-Based Online Grid Impedance Identification With Grid-Tied Converters

Zipeng Liu, *Student Member, IEEE*, Jinjun Liu, *Fellow, IEEE*, and Zeng Liu, *Member, IEEE*

***Abstract*—Grid impedance information occupies a fundamental and crucial position for the operation of grid-tied converters. Consequently, accurate and fast extraction of grid impedance is vital. The impulse injection method applied under the control loop of a grid-tied converter, which is commonly used to extract linear grid impedance online, is relatively reasonable in terms of device cost, measurement speed, simplicity, and design flexibility. However, the selection of impulse and design of impulse parameters mostly depend on rules of thumb, without theoretical guidance, leading to insufficient measurement accuracy in target frequency section and greatly burdening the system. To address these issues, a systematic guidance is proposed for analysis, design, and implementation of impulse-injection-based grid impedance identification. By comparing the spectra of several basic impulses with unipolar and bipolar forms and analyzing the impact when impulse parameters are altered, a guidance for impulse selection for different measurement scenarios is presented. Based on this guidance, an asymmetric bipolar sawtooth wave with a defined asymmetry ratio of $\rho = 0.5$ is chosen in this article for broadband measurement of grid impedance. Furthermore, a related parameter design procedure with optimal injection position and instant is also proposed to reduce system burden and eliminate overmodulation when injecting the impulse. Finally, theoretical results are validated by experiments.**

***Index Terms*—Impedance measurement, impulse injection method, power electronics systems.**

I. Introduction

UNDER the trend of electronic and intelligent, contemporary power systems are incorporating a growing number of power electronics devices. Although these devices provide prominent performance, the interaction between devices and grid might cause system instability [1]. To predict stability and optimize system design, a series of impedance-based criteria for grid-tied inverter systems have been proposed; these include the Middlebrook criterion [2], forbidden region theory [3], [4], singular-value criterion [5], and infinity-norm criterion [6], etc. While all these criteria give designers maximum flexibility to predict stability, impedance information plays a crucial role in this process, leading to attention being focused on fast and accurate measurement methods.

Various measurement methods have been proposed for dc and ac distributed power systems (DPSs). According to the implementation method of perturbation, existing impedance measurement methods can be grouped into two categories: measurement with external perturbation injectors and measurement without external perturbation injectors. The first type is implemented by shunt current injectors or series voltage injectors using single-phase or three-phase injection and line-to-line injection [7]–[11], and the related signal pattern is usually the traditional sweep method [12]. The compound signals such as multitone or pseudorandom sequence (PRS) can also be used in some scenarios [13], [14]. Extraction with an external perturbation injector is usually accurate, but the high cost of its equipment is a prominent problem, and it also takes a long time to complete the measurement when sweep method is applied. For the second type, a grid-tied converter or load is employed to generate the required perturbations by load steps or impulse injection [15], [16], where the signal pattern is usually the compound signals such as pseudorandom binary sequence (PRBS) [17], [18], transient state and impulse [19]. Since this kind of method uses the existing equipment in the system, no extra investment is needed, which significantly reduces the cost of measurement. Meanwhile, using the compound signals can also ensure the real-time measurement of grid impedance.

For compound signals, the PRS attracts more attention due to its optimal crest factor, with which the PRS can identify the system without significantly disturbing the system, i.e., the maximum-length binary sequence shows a good applicability for sensitive systems [20]. But several practical issues should also be carefully considered, including the time-aliasing error [21], consideration of signal length and injection period [22], [23], etc. Unlike the PRS, the impulse has a high simplicity in its usage. At the same time, it has the shortest measurement time in theory and has the flexibility to adjust the distribution of spectrum. The poor crest factor is its prominent issue.

Given the disturbance source and signal pattern, the impulse injection method without external perturbation injectors is relatively reasonable in terms of device cost, measurement speed,

Manuscript received August 27, 2019; revised January 20, 2020; accepted May 1, 2020. Date of publication May 14, 2020; date of current version July 31, 2020. This work was supported by the National Natural Science Foundation of China under Grant 51437007. Recommended for publication by Associate Editor R. Burgos. *(Corresponding author: Zeng Liu.)*

The authors are with the State Key Laboratory of Electrical Insulation and Power Equipment, School of Electrical Engineering, Xi'an Jiaotong University, Xi'an 710049, China (e-mail: liuzipeng.pe@foxmail.com; jjliu@mail.xjtu.edu.cn; zengliu@mail.xjtu.edu.cn).

Color versions of one or more of the figures in this article are available online at https://ieeexplore.ieee.org.

Digital Object Identifier 10.1109/TPEL.2020.2995016

design flexibility and especially the simplicity, and can meet most application scenarios in grid impedance measurement. But the poor crest factor should be carefully treated.

Initial implementation of the impulse injection method without external perturbation injectors was realized by cutting in and off the capacitor or inductor in the system [24]–[26]. The transient state can be approximated as a triangular impulse, which contains a series of harmonics, and can enable instantaneous measurement. This method is simple and easy to implement, but it greatly interferes with normal operation of system. Meanwhile, the generated impulse completely depends on the system characteristics, whereby the spectrum of the impulse is totally uncontrollable, which affects the accuracy of measurement results.

Changing the active and reactive power can also be utilized in the impulse injection method [27], [28]. By adjusting the output active and reactive power of the grid-tied converter, the impedance of the transmission line can be obtained by a simple calculation without the need to perform the fast Fourier transform (FFT) analysis, whereby the computation burden is obviously reduced. However, this method requires the assumption that the tested objects are series resistor and inductor and cannot meet other measurement scenarios.

A more flexible and controllable impulse injection method is applied under the control loop of the grid-tied converter. By adding the designed impulse to the reference in the control loop, the grid-tied converter will trace the reference to output the target impulse [16], [19], [29]–[35]. This method utilizes the existing grid-tied converter and makes flexible use of the control loop, whereby the parameters of the impulse, such as the width, magnitude, and injection instant, are completely controllable. Because the injection duration is extremely short, the system transient process caused by the impulse is also extremely short, which can reduce the system burden.

Compared with the other two types of methods, the impulse injection method applied under the control loop has attracted more attention because of its significant technical merits. When calculating the impedance of linear systems, the correlation method can be used to obtain higher precision than the traditional FFT [33]. The Prony method can also be used to deal with the influence of nonlinear loads when measuring the linear loads, but it is susceptible to noise [19], [33]. Embedding this method into the controller of the grid-tied inverter to realize real-time monitoring and optimize adaptive control has also been well discussed [31], [36].

However, in addition to its technical superiorities, this method also suffers from several serious issues. First, the selection of the impulse mostly depends on rules of thumb, without theoretical guidance, in which condition the accuracy of the measurement results cannot be expected [37]. Different impulses have diverse spectrum characteristics, leading to unequal signal to noise ratio (SNR) and measurement accuracy. The selection of impulse should follow a reliable guidance to achieve optimal performance under different measurement scenarios. Second, injected impulse may exceed the system rating for its poor crest factor [31]. The impulse will superimpose on three-phase currents and voltages. If the impulse parameters such as magnitude and injection instant are not well designed, the perturbed three-phase variables may exceed the system rating. Moreover, it was observed that the injected impulse can suffer from uncontrolled distortion as a result of overmodulation, which may affect the accuracy of measurement results. The impulse will be injected into the control loop and superimposed onto the original control signal, in which process of the new control signal may get out of the linear region of pulsewidth modulation (PWM) generator and cause overmodulation, leading to impulse distortion and other system problems.

Aiming at aforementioned issues, this article proposes an impulse selection and design method for impulse-injection-based grid impedance measurement. Its contribution can be summarized as follows. First, an impulse selection guidance is proposed. The Fourier analysis is performed to compare the different characteristics for several basic impulses with unipolar and bipolar forms, and discuss the impact of changing impulse parameters, whereby an impulse selection guidance is proposed for certain application scenarios. Based on this guidance, an asymmetric bipolar sawtooth wave with a defined asymmetry ratio of $\rho = 0.5$ is chosen in this article for broadband measurement of grid impedance. Second, a detailed parameter design procedure for chosen impulse has been established to reduce system burden and further improve measurement accuracy based on the optimal injection position and instant. Besides, practical issues of data processing are also discussed.

The rest of this article is arranged as follows. The generalized implementation of impulse-injection-based online grid impedance identification is presented in Section II. The comparison and analysis of the impulse spectrum are presented in Section III. The parameter design procedure based on the chosen impulse is summarized in Section IV. Section V investigates the proposed design method by experimental testing, and practical issues of data processing are also discussed in this section. Finally, the conclusion is presented in Section VI.

II. Generalized Implementation of Impulse-Injection-Based Online Grid Impedance Identification

Impedance extraction requires rational and accurate modeling of impedance. For linear systems, the impedance is defined as $U\angle\theta/I\angle\varphi$. For nonlinear systems, the impedance is defined as small-signal impedance around a certain steady-state operating point. The grid impedance is usually considered to be linear. In some cases, the grid side contains a nonlinear load with a relatively low power rating, at which point the grid side is also considered as weakly nonlinear or nearly linear. For linear or weakly nonlinear grid impedance, measurement methods based on small-signal linearization are always effective.

The generalized implementation of the impulse injection method applied under control loop with a grid-tied inverter is realized by injecting a basic impulse, such as a triangular or square wave, onto the reference of the current or voltage. As shown in Fig. 1, by injecting an impulse on the α-axis of the current reference, the output current of the PWM converter on a-axis would be superimposed with a similar impulse, which

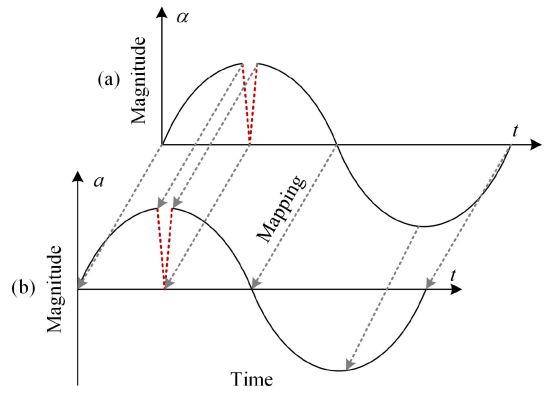

Fig. 1. Impulse injection on (a) the α-axis and (b) the a-axis.

contains a series of harmonics with different amplitudes. After FFT processing of the pertinent voltage and current disturbances, the impedance information over the target frequency section can be easily worked out.

The sampled data can be directly processed under the stationary abc reference frame, especially for grid impedance, which is often considered to be balanced and symmetrical in practice. In this case, the single-phase impedance model is usually adopted.

A. Grid-Tied Inverter System and Impulse Injection

A typical grid-tied inverter system is shown in Fig. 2. The impulse is injected on the α-axis, where the three-phase PWM inverter is controlled as a current source, and the corresponding proportional-resonant (PR) controller is used for single-loop current control. Current and voltage sensors are located at the interface, and with these the measured data can be used for phase-lock and impedance measurement. With the phase information θ provided by the synchronous reference frame (SRF) phase-locked loop (PLL), the $dq/\alpha\beta$ transformation can be synchronized with the fundamental frequency. θ can also be used to control the injection instant of impulse, i.e., if θ equals to designed injection angle, θ^*, then the impulse will be injected onto the control loop. In other cases, a proportional-integral controller can also be employed to realize the control under a synchronous dq reference frame, and the control method is also adjusted accordingly.

B. Data Extraction and Calculation

After measurement of the resultant voltages and currents, an extraction method called steady-state compensation method can be applied to obtain the actual impulse [38]. The main idea is to use the measured voltage and current to subtract the corresponding steady-state value, whereby the fundamental frequency component and the background noise or harmonics can be eliminated. Thus

$$\begin{aligned} v'(t) &= v_m(t) - v_s(t) \\ i'(t) &= i_m(t) - i_s(t) \end{aligned} \tag{1}$$

where v_m and i_m are the measured data, v_s and i_s are the steady-state data, and v' and i' are the compensated data.

It should be mentioned that the measured data and the steady-state data should be synchronized, which means that the data should start with the same phase angle. Then, the FFT analysis, $\mathcal{F}(\cdot)$, can be directly applied on the compensated data, so

$$Z_g(f) = \frac{\mathcal{F}(v'(t))}{\mathcal{F}(i'(t))}. \tag{2}$$

For real-time monitoring of the grid impedance, the data should be measured by embedded sensors in the system. Similar data processing and calculation will be implemented in the digital signal processor. To increase the calculation speed, a sliding discrete Fourier transform (DFT) or half-length complex-valued DFT can be utilized [31], [39].

C. Influence of PLL Angle Deviation

When grid-tied converter is controlled under the stationary $\alpha\beta$ reference frame, the reference values are always synchronized with point of common coupling (PCC) voltage by PLL. But the injected impulse may affect the synchronization. The injected impulse, which is added onto the reference value, will be output by grid-tied converter as a current perturbation, and further induce a voltage disturbance at PCC point. This voltage disturbance in turn adds a small deviation onto the PLL angle, which may affect the synchronization.

Let $\mathbf{i}^*_{\alpha\beta}$ denote the ideal reference values without the influence of PLL angle deviation, and $\mathbf{i}'_{\alpha\beta}$ denote reference values with the influence of PLL angle deviation. When system is free of injection, the PLL angle is always synchronized with PCC voltage, so $\mathbf{i}'_{\alpha\beta}$ should be equal to $\mathbf{i}^*_{\alpha\beta}$. Thus

$$\mathbf{i}^*_{\alpha\beta} = \begin{bmatrix} i^*_\alpha \\ i^*_\beta \end{bmatrix} = \begin{bmatrix} \cos(\theta) & -\sin(\theta) \\ \sin(\theta) & \cos(\theta) \end{bmatrix} \begin{bmatrix} i^*_d \\ i^*_q \end{bmatrix} = \mathbf{i}'_{\alpha\beta} \tag{3}$$

where θ is output angle of PLL, i^*_d and i^*_q are constant reference values under the dq reference frame. This relationship can also be represented as follows:

$$\begin{bmatrix} i'_\alpha \\ i'_\beta \end{bmatrix} = \begin{bmatrix} \cos(0) & -\sin(0) \\ \sin(0) & \cos(0) \end{bmatrix} \begin{bmatrix} i^*_\alpha \\ i^*_\beta \end{bmatrix}. \tag{4}$$

When a small-signal perturbation, $\tilde{\theta}$, is added onto the PLL angle, and let $\theta' = 0 + \tilde{\theta}$, the small-signal model is

$$\begin{bmatrix} i'_\alpha + \tilde{i}'_\alpha \\ i'_\beta + \tilde{i}'_\beta \end{bmatrix} = \begin{bmatrix} \cos(\theta') & -\sin(\theta') \\ \sin(\theta') & \cos(\theta') \end{bmatrix} \begin{bmatrix} i^*_\alpha + \tilde{i}^*_\alpha \\ i^*_\beta + \tilde{i}^*_\beta \end{bmatrix}. \tag{5}$$

Use small angle approximation of trigonometric function, and cancel the steady-state values, the model becomes

$$\begin{bmatrix} i'_\alpha + \tilde{i}'_\alpha \\ i'_\beta + \tilde{i}'_\beta \end{bmatrix} \approx \begin{bmatrix} 1 & -\tilde{\theta} \\ \tilde{\theta} & 1 \end{bmatrix} \begin{bmatrix} i^*_\alpha + \tilde{i}^*_\alpha \\ i^*_\beta + \tilde{i}^*_\beta \end{bmatrix}, \tag{6}$$

$$\begin{bmatrix} \tilde{i}'_\alpha \\ \tilde{i}'_\beta \end{bmatrix} \approx \begin{bmatrix} \tilde{i}^*_\alpha - \tilde{\theta} \cdot i^*_\beta \\ \tilde{i}^*_\beta + \tilde{\theta} \cdot i^*_\alpha \end{bmatrix}. \tag{7}$$

For SRF-PLL, its proportional-integral controller is

$$H_{pll} = k_p^{pll} + \frac{k_i^{pll}}{s} \tag{8}$$

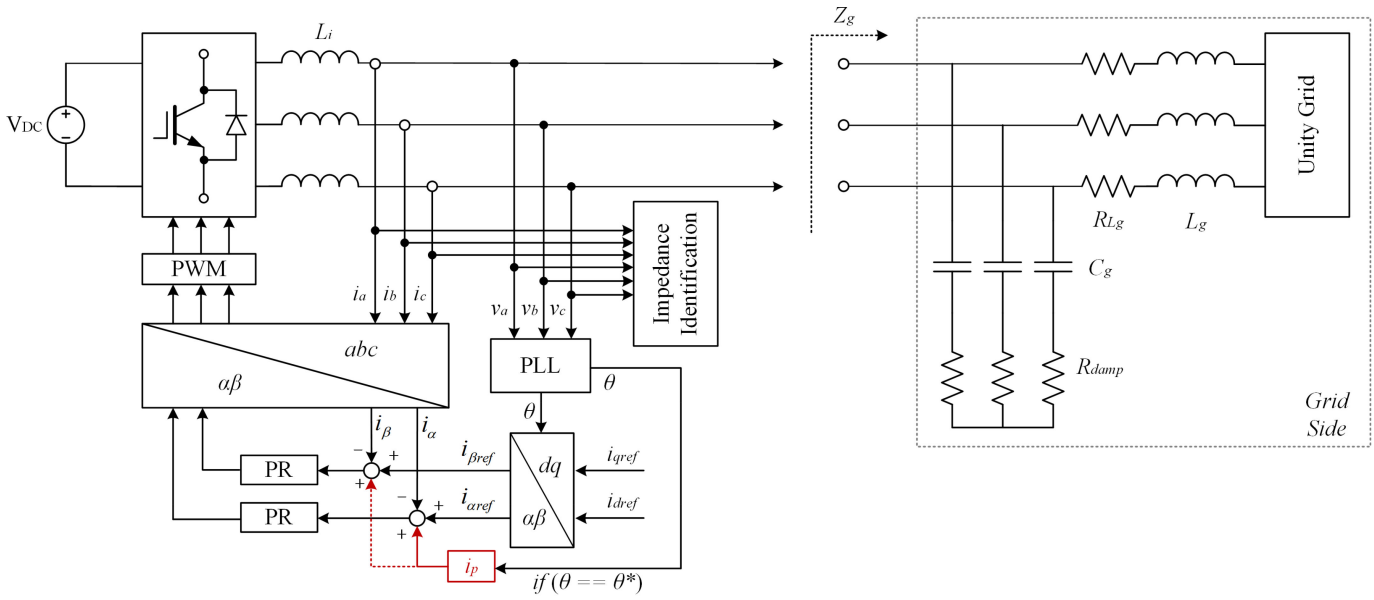

Fig. 2. Typical grid-tied inverter system for impulse injection. The impulse i_p is injected on the α- or β-axis and will be mapped to all three phases with different ratios, while the grid-tied inverter will output the designed impulse as a current impulse.

where k_p^{pll} and k_i^{pll} are proportional and integral coefficients, respectively.

The angle deviation, $\tilde{\theta}$, can be expressed as follows [40]:

$$\tilde{\theta} = G_{pll} \cdot \tilde{v}_q^s \tag{9}$$

where $\tilde{v}_q^s$ is the voltage disturbance at PCC point under the q-axis, and G_{pll} is defined as follows:

$$G_{pll} = \frac{H_{pll}}{s + V_d^s H_{pll}} \tag{10}$$

where V_d^s is the steady-state voltage at PCC point under the d-axis. Hence

$$\begin{aligned} \begin{bmatrix} \tilde{i}'_\alpha \\ \tilde{i}'_\beta \end{bmatrix} &\approx \begin{bmatrix} \tilde{i}^*_\alpha - G_{pll} \cdot \tilde{v}_q^s \cdot i^*_\beta \\ \tilde{i}^*_\beta + G_{pll} \cdot \tilde{v}_q^s \cdot i^*_\alpha \end{bmatrix} \\ &= \underbrace{G_{pll} \begin{bmatrix} -i^*_\beta \tilde{v}_q^s \\ i^*_\alpha \tilde{v}_q^s \end{bmatrix}}_{\text{error}} + \begin{bmatrix} \tilde{i}^*_\alpha \\ \tilde{i}^*_\beta \end{bmatrix}. \end{aligned} \tag{11}$$

Equation (11) shows that, the actual reference value $\mathbf{i}'_{\alpha\beta}$ is different from the ideal one, $\mathbf{i}^*_{\alpha\beta}$. Obviously, the error can be regarded as some signals passing through a filter, G_{pll}. Fig. 3 shows the characteristics of H_{pll} and G_{pll} under certain parameters. It can be observed that the gain of G_{pll} is extremely low due to the reason that the V_d^s affects the characteristics of G_{pll} prominently, as shown in (10). Therefore, the error between $\mathbf{i}'_{\alpha\beta}$ and $\mathbf{i}^*_{\alpha\beta}$ will be significantly suppressed. For this reason, the influence of PLL angle deviation can be ignored to simplify the further analysis.

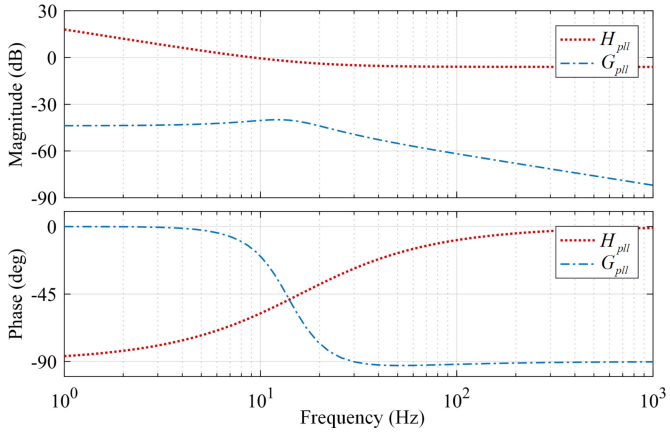

Fig. 3. Bode diagram of H_{pll} and G_{pll}. The parameters are: $k_p^{pll} = 0.5$, $k_i^{pll} = 50$, $V_d^s = 155$ V.

D. Impulse Requirements

For grid impedance measurement, the impulse should follow the following three basic rules.

1) The impulse should be high enough to get a high SNR but not be too high to disturb normal operation of the system.
2) The impulse should be short enough so that the system parameters can be treated as static over that duration.
3) The spectrum of impulse should cover the target frequency section. The bandwidth up to $1/2$ switching frequency is preferred, and usually hundreds or thousands of hertz.

Meanwhile, to guarantee system stability and power quality, the current loop is always well designed with a limited bandwidth, which will reduce the spectrum of the chosen impulse

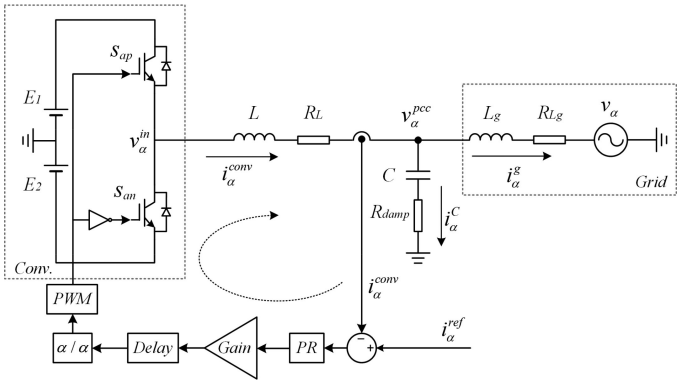

Fig. 4. Structure of the studied grid-connected system in the α/α axis.

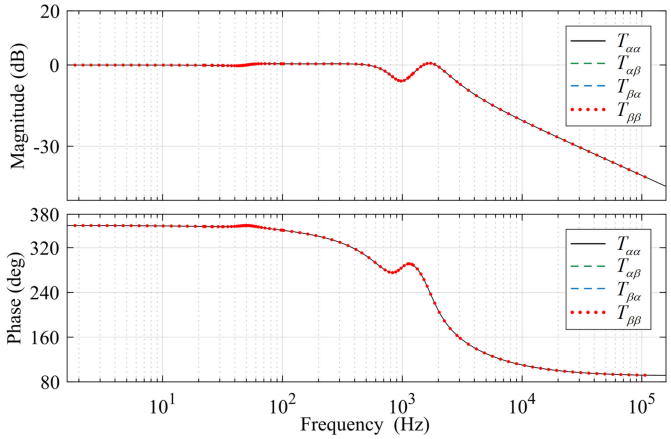

Fig. 5. Bode diagram of the four closed-loop transfer functions of the current loop with the chosen parameters, including α/α, β/β, α/β, and β/α.

in the high-frequency section. This high-frequency rejection property should also be considered.

To simplify the analysis, take the α/α axis as an example. The system structure is shown in Fig. 4, where v_α^{pcc} represents the voltage of the PCC on the α-axis, R_{damp} is the damping resistor, and R_L and R_{Lg} are the equivalent series resistors. The influence of system PWM delay is also considered in this article. The α/α block represents the mathematical mapping relationship between the two axes. Based on this block diagram, the system can be modeled as follows:

$$\begin{cases} \left(i_\alpha^{\text{ref}} - i_\alpha^{\text{conv}}\right) G_t = v_\alpha^{\text{in}} \\ v_\alpha^{\text{pcc}} + i_\alpha^{\text{conv}} \left(sL + R_L\right) = v_\alpha^{\text{in}} \\ i_\alpha^C \left(\frac{1}{sC} + R_{\text{damp}}\right) = v_\alpha^{\text{pcc}} \\ i_\alpha^{\text{conv}} - i_\alpha^C = i_\alpha^g \\ v_\alpha^{\text{pcc}} - i_\alpha^g \left(sL_g + R_{Lg}\right) = v_\alpha \end{cases} \tag{12}$$

where $G_t = G_{\text{PR}} G_{\text{delay}} G_{\text{gain}} G_{\text{PWM}} G_{\alpha/\alpha}$.

The following nonideal PR controller is adopted in this research [41]:

$$G_{\text{PR}} = k_P + \frac{2k_R \omega_c s}{s^2 + 2\omega_c s + \omega_r^2} \tag{13}$$

where k_P and k_R are proportional and resonance coefficients, respectively, and ω_r and ω_c are resonant and passband cutoff frequencies, respectively.

The system PWM delay can be expressed as follows [42]:

$$G_{\text{delay}} \approx \frac{1 - 0.75T_s s}{1 + 0.75T_s s} \tag{14}$$

where T_s is the system control cycle.

The PWM modulation process can be treated as proportional amplification or minification, where

$$G_{\text{PWM}} = \frac{V_{\text{DC}}}{2} \tag{15}$$

$$G_{\text{gain}} = \frac{2}{V_{\text{DC}}}. \tag{16}$$

Let $Z_C = \frac{1}{sC} + R_{\text{damp}}$, $Z_{Lg} = sL_g + R_{Lg}$, and $Z_L = sL + R_L$, so the current closed-loop transfer function of grid-tied system on α/α axis is as follows:

$$T_{\alpha\alpha} = \frac{\hat{i}_\alpha^{\text{conv}}}{\hat{i}_\alpha^{\text{ref}}} = \frac{G_t}{\frac{Z_C Z_{Lg}}{Z_C + Z_{Lg}} + Z_L + G_t}. \tag{17}$$

TABLE I
PARAMETERS OF CURRENT CLOSED-LOOP TRANSFER FUNCTION

Parameter	Value	Parameter	Value
C	15 μF	k_P	20
R_{damp}	5 Ω	k_R	1000
L_g	1.75 mH	ω_r	100π
R_{Lg}	0.01 Ω	ω_c	π
L	3.5 mH	T_s	0.1 ms
R_L	0.01 Ω	G_{gain}	1/200
V_{DC}	200 V	α/α	1

According to (17), a bode diagram can be drawn under certain parameters. Fig. 5 shows the bode diagram of four closed-loop transfer functions, where α/α and β/β are the same, and α/β and β/α are zero because the two axes, α and β axes, are decoupled from each other when PLL is ignored. In this condition, the system can be treated as symmetric. The parameters chosen in this article are summarized in Table I.

To increase the SNR in the high-frequency section and ensure the measurement accuracy, an impulse should have a higher magnitude in the high-frequency section to reduce the effect of the current closed-loop. This should also be an important rule for impulse selection.

III. Comparison and Analysis of Impulse Spectrum

Impulse selection should follow the basic rules discussed in Section II. Consider the distribution of harmonics and background noise in power electronics systems: Noise is distributed throughout the whole frequency band with decreasing amplitude, with the majority of noise scattered in the middle- and high-frequency section, especially in the 100 Hz $-$ -1 kHz range. To guarantee a high SNR, the spectrum of the chosen impulse should better have a similar distribution. Certainly, a wide variety of impulses with this distribution can be used in measurement,

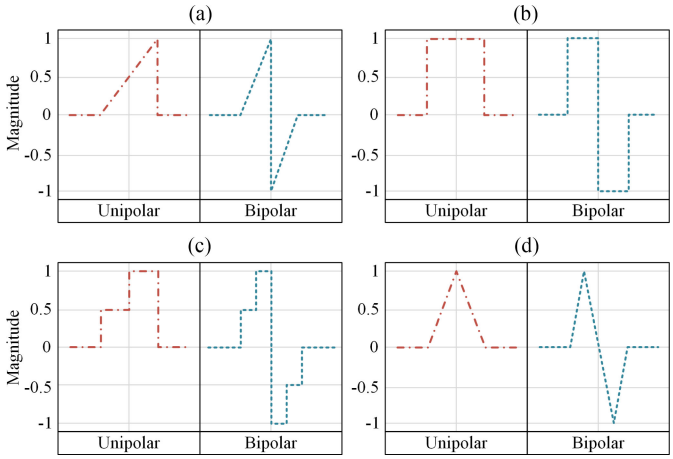

Fig. 6. Unipolar (dot dash line) and symmetric bipolar (dotted line) waveforms of basic impulses: (a) sawtooth wave, (b) square wave, (c) step wave, (d) triangular wave.

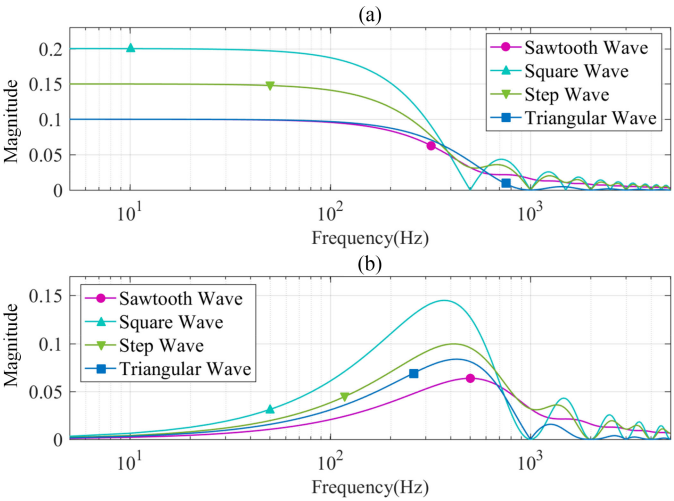

Fig. 7. FFT analysis of (a) unipolar and (b) symmetric bipolar basic impulses with the same parameters, i.e. an magnitude of 10 and a duration of 0.002 s under the FFT window width of 0.2 s.

however, to simplify the design of impulse parameters, basic impulses that can be described by a simple equation and easily applied in the embedded controller will be discussed in this article.

A. Spectrum Comparison of Basic Impulses

Basic unipolar and bipolar impulses, including sawtooth, square, step, and triangular waves, are the most commonly used impulses in engineering. They are easy to design, and parameters are easy to adjust owing to the simple and structured waveform, as shown in Fig. 6. To compare the applicability of these impulses, spectra will be compared for case where the impulses have the same magnitude and duration.

As can be seen from Fig. 7, the unipolar impulses distribute majority of their energy in the low-frequency section where the system spreads less noise. When SNR is higher than a certain value, spreading more energy in low-frequency section is unnecessary. In this case, symmetric bipolar impulses exhibit a better distribution feature that nearly aligns with the distribution of noise.

TABLE II
IMPULSE CHARACTERISTICS

	Advantages	Drawbacks	Measurement
Square wave	Highest magnitude in EB	Zero points in spectrum	Narrow bandwidth measurement
Sawtooth wave	No zero points in spectrum	Lower magnitude	Broadband measurement
Triangular wave	Low dynamic performance requirement	Zero points in spectrum	System with poor dynamic performance

It is obvious that the step wave is the real output waveform of the sawtooth wave when the latter is injected into a digital controlled system. Theoretically, an infinite-order step wave is equal to a sawtooth wave. In this article, the switching frequency of the insulated-gate bipolar transistors is high enough so that the generated sawtooth wave will turn out to be a high-order step wave. Owing to the similarity of the sawtooth wave and the high-order step wave, the latter one will not be discussed in the following.

The characteristics for each impulse are summarized in Table II, where the effective bandwidth (EB) means 0 Hz to the next zero point in its spectrum. To measure the impedance over a wide bandwidth, the sawtooth wave will be chosen in this article.

B. Theoretical Analysis of Bipolar Impulses

Different types of bipolar impulses have dissimilar properties, making them suited for different measurement conditions. To gain a better understanding of spectrum of bipolar impulses, especially the square and sawtooth waves, it is very important to discuss the influence of the impulse parameters on spectrum characteristics.

Generally, for arbitrary $x(t)$, the Fourier transformation is defined as follows:

$$\mathcal{F}\{x(t)\} = X(j\Omega) = \left\langle x(t), e^{j\Omega t} \right\rangle. \tag{18}$$

When the magnitude changes, we let $x(t) \to ax(t)$, so

$$X'(j\omega) = aX(j\Omega) \tag{19}$$

which means that, when the magnitude of impulse increases a times, the spectrum will also increase a times.

When the width changes, we let $x(t) \to x(at)$, and $\tau = at$, so

$$\mathcal{F}\{x(at)\} = \begin{cases} \frac{1}{a}\left\langle x(\tau), e^{j\left(\frac{\Omega}{a}\right)\tau} \right\rangle, & a > 0 \\ -\frac{1}{a}\left\langle x(\tau), e^{j\left(\frac{\Omega}{a}\right)\tau} \right\rangle, & a < 0. \end{cases} \tag{20}$$

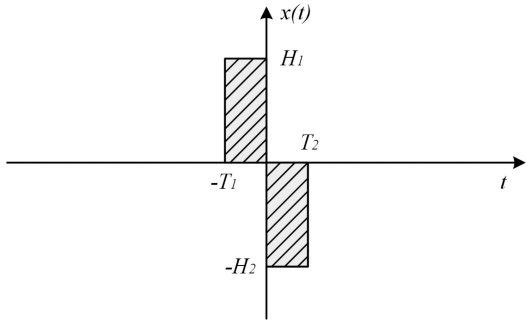

Fig. 8. Bipolar square wave with parameter definitions in the time domain.

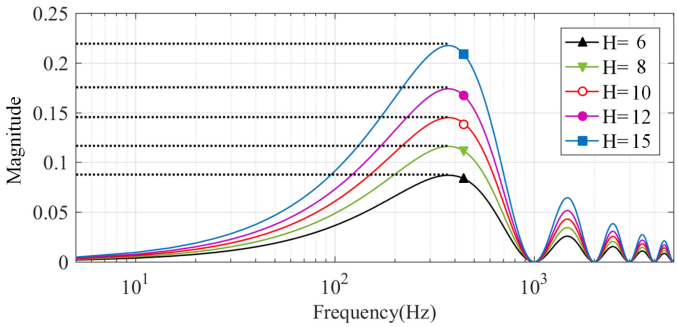

Fig. 9. Spectrum of symmetric bipolar square waves with unified width of 0.002 s and different magnitudes H under the FFT window width of 0.2 s. It is obvious that when impulse magnitude increases n times, the spectrum will also increase n times.

This can also be represented as follows:

$$X'(j\omega) = \frac{1}{|a|} X\left(\frac{j\Omega}{a}\right) \tag{21}$$

which means that, when the width of impulse increases a times, the spectrum will also increase $|a|$ times, but the EB will decrease to $1/a$.

These two properties are suited for arbitrary waveforms. In the rest of this section, the properties are summarized as the *spectrum change law*.

1) Parameter Analysis of the Bipolar Square Wave: The bipolar square wave will be discussed first for it is the simplest waveform to describe. Consider a continuous and aperiodic bipolar square wave in time domain, with single injection, as shown in Fig. 8.

Using the Fourier transformation, the selected impulse can be transformed into the frequency domain as follows:

$$X(j\omega) = \frac{H_1}{j\omega} e^{j\omega T_1} + \frac{H_2}{j\omega} e^{-j\omega T_2} - \frac{H_1 + H_2}{j\omega}. \tag{22}$$

When the bipolar square wave is totally symmetrical, we let $H_1 = H_2 = H$, and $T_1 = T_2 = T$, so, (22) can be simplified to

$$X(j\omega) = \frac{2H}{j\omega} [\cos(\omega T) - 1]. \tag{23}$$

Equation (23) follows the spectrum change law. Figs. 9 and 10 show these two properties. Equation (23) also demonstrates that the zero-magnitude points in the spectrum are arranged as

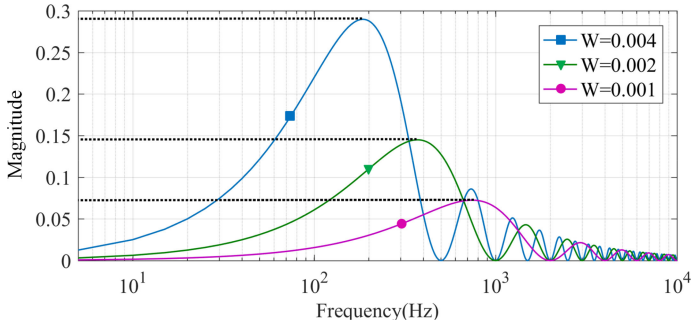

Fig. 10. Spectrum of symmetric bipolar square waves with unified magnitudes of 10 and different impulse width W under the FFT window width of 0.2 s. It is obvious that when the impulse width increases n times, the spectrum will also increase n times, and the EB will decrease to $1/n$.

follows:

$$f_0 = \frac{n}{T},\ n \in Z \tag{24}$$

where T is half of the impulse duration. In this equation, let $n = 1$, then EB can be calculated.

It can be observed in Figs. 9 and 10 that the symmetric bipolar square wave has a very low magnitude in the low-frequency section. The basic reason for this is that the dc component of the two poles cancels each other. The spectrum cannot ensure a high SNR in the low-frequency section, especially in systems with background noise. To get a higher magnitude in the low-frequency section, the asymmetric bipolar wave is considered.

Let $H_1 = H_2 = H$ and $T_1 \neq T_2$. Then, (22) can be simplified to

$$X(j\omega) = \frac{H}{j\omega} \left(e^{j\omega T_1} + e^{-j\omega T_2} - 2\right). \tag{25}$$

Equation (25) follows the spectrum change law. Assume $T_2 = a \cdot T_1, a \in Z^+$, and $T_2 > T_1$, so the zero points in spectrum are decided by

$$f_0 = \frac{n}{T_1},\ n \in Z^+ \tag{26}$$

and Fig. 11 shows this property.

When $T_1 = T_2 = T$ and $H_1 \neq H_2$, (22) can be simplified to

$$X(j\omega) = \frac{H_1}{j\omega} e^{j\omega T} + \frac{H_2}{j\omega} e^{-j\omega T} - \frac{H_1 + H_2}{j\omega}. \tag{27}$$

Equation (27) follows the spectrum change law. Assume $H_2 = nH_1, n \in R^+$; then the zero point is also decided by (24). Fig. 12 shows this property.

Obviously, the asymmetric bipolar square wave spreads more energy in the low-frequency section than the symmetric one, being better suited for practical system measurement with background noise.

2) Parameter Analysis of the Bipolar Sawtooth Wave: The analysis of a bipolar sawtooth wave follows the same method as in the previous part. Let the bipolar sawtooth wave be continuous and aperiodic, as shown in Fig. 13.

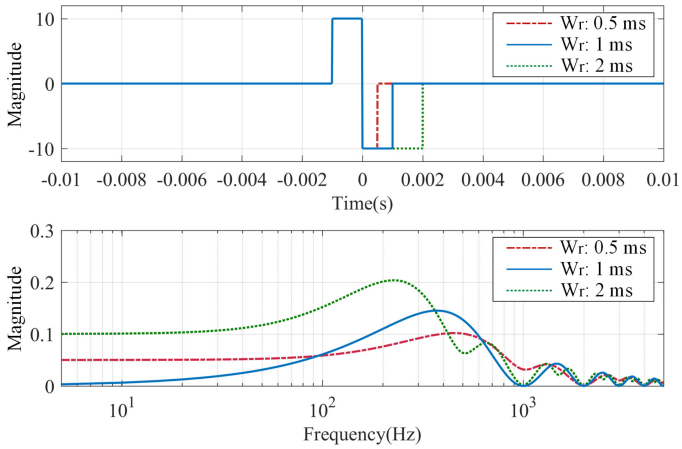

Fig. 11. Spectrum of asymmetric bipolar square waves with unified magnitudes of 10 and unequal polar widths under the FFT window width of 0.2 s. W_r denotes the width of right pole.

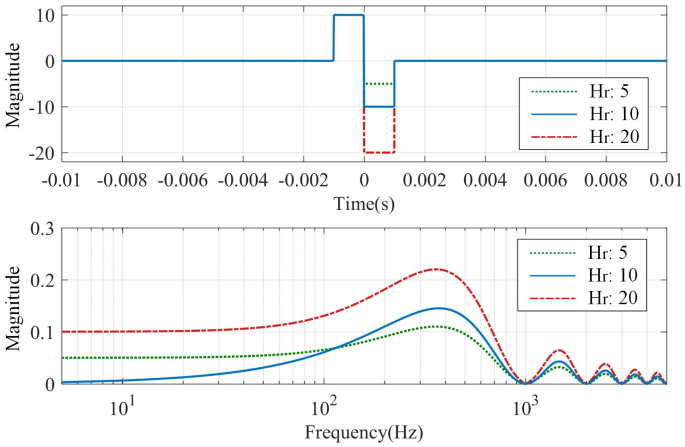

Fig. 12. Spectrum of asymmetric bipolar square waves with unified width of 0.002 s and unequal polar magnitudes under the FFT window width of 0.2 s. H_r denotes the magnitude of right pole.

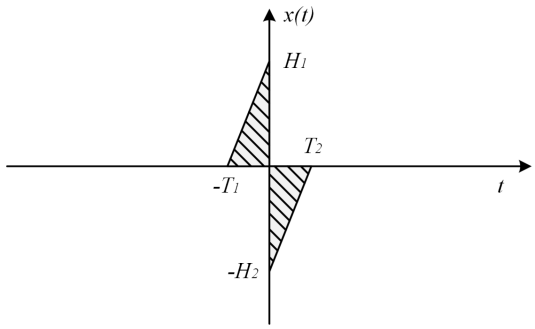

Fig. 13. Bipolar sawtooth wave with parameter definitions in the time domain.

With the parameter definitions, the chosen impulse can be transformed into frequency domain. The analytical equation is

$$X(j\omega) = \frac{H_1}{\omega^2 T_1} - \frac{H_2}{\omega^2 T_2} - \frac{H_1+H_2}{j\omega} - \frac{H_1 e^{j\omega T_1}}{\omega^2 T_1} + \frac{H_2 e^{-j\omega T_2}}{\omega^2 T_2}. \tag{28}$$

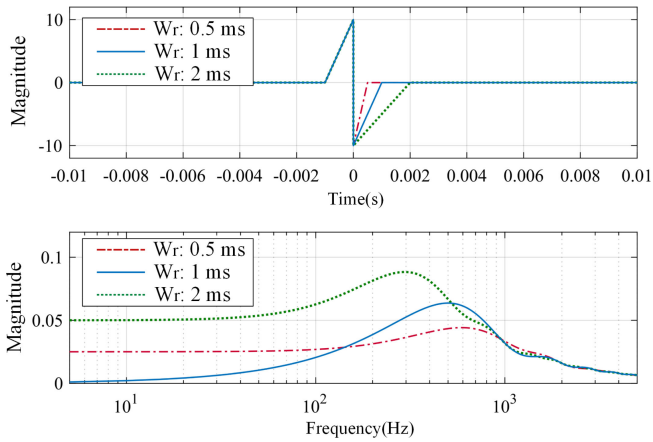

Fig. 14. Spectrum of asymmetric bipolar sawtooth waves with unified magnitudes of 10 and unequal polar widths under the FFT window width of 0.2 s. W_r denotes the width of right pole.

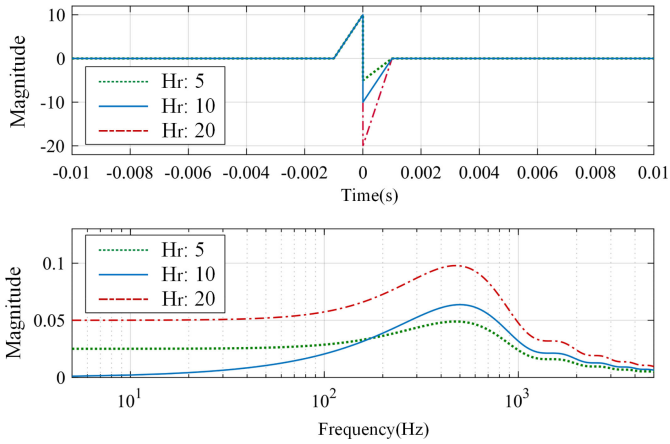

Fig. 15. Spectrum of asymmetric bipolar sawtooth waves with unified widths and unequal polar magnitudes under the FFT window width of 0.2 s. H_r denotes the magnitude of right pole.

Similarly, when the bipolar sawtooth wave is symmetrical or asymmetrical with unequal width or magnitude, (28) can be simplified to the following forms, accordingly:

$$X(j\omega) = \frac{2H}{j\omega}\left[\frac{\sin(\omega T)}{\omega T} - 1\right] \tag{29}$$

$$X(j\omega) = H\left(\frac{1-e^{j\omega T_1}}{\omega^2 T_1} - \frac{1-e^{-j\omega T_2}}{\omega^2 T_2} - \frac{2}{j\omega}\right) \tag{30}$$

$$X(j\omega) = \frac{H_1\left(1-e^{j\omega T}\right) - H_2\left(1-e^{-j\omega T}\right)}{\omega^2 T} - \frac{H_1 + H_2}{j\omega}. \tag{31}$$

Equations (29)–(31) also follow the spectrum change law and have no zero points when $0 < \omega < \infty$, which makes the sawtooth wave more suitable for broadband measurement. Spectral characteristics can be observed in Figs. 14 and 15. It is easier to use the asymmetric form with unequal magnitude. Define the asymmetry ratio ρ as the ratio of the magnitude of the right pole

TABLE III
COMPARISON OF IMPULSE FORMS

	Unipolar	Bipolar	
Form	—	Symmetric	Asymmetric
Advantages	More energy in low-frequency band	More energy in middle- and high-frequency bands	Rational distribution in full band
Drawbacks	Low energy in high-frequency band	Low energy in low-frequency band	—

to the left pole where $H_{\text{right}} < H_{\text{left}}$ and it satisfies

$$\rho = \frac{H_{\text{right}}}{H_{\text{left}}},\ \rho \in (0,1)\,. \tag{32}$$

When ρ approaches 1, the impulse is similar to a symmetric bipolar impulse. When ρ approaches 0, the impulse is similar to a unipolar impulse. The asymmetric bipolar sawtooth wave with $\rho = 0.5$ is chosen in this article for broadband measurement. $\rho = 0.5$ is a moderate choice, which can also be adjusted to other values to meet different measurement requirements. A comparison of unipolar, symmetric bipolar, and asymmetric bipolar waves is summarized in Table III. The selection of impulse can be referred to Tables II and III for different scenarios.

IV. PARAMETER DESIGN OF IMPULSE INJECTION BASED ON ASYMMETRIC BIPOLAR SAWTOOTH WAVE

According to the impulse spectrum analysis, the asymmetric bipolar sawtooth wave is chosen for broadband measurement. Because of its unique waveform, it can more easily exceed the system rating. To guarantee that the current and voltage are always in the secure region of the system, parameter design of the impulse becomes a practical issue in this application.

The impulse parameters include the width, magnitude, injection position, and injection instant. The width can be designed separately, while the other three are related factors. According to (24) and (26), the width of impulse can be decided by EB to cover the frequency range of measurement. For example, a symmetry bipolar square wave with width equal to 4 ms has a 500 Hz EB, which means it can be used for measurement from 0 to 500 Hz. For sawtooth wave, although no zero point exists in its spectrum, but the spectrum distribution trend is totally consistent with the square wave. So, (24) and (26) can also be used to estimate the main spectrum distribution section of sawtooth wave with certain width, i.e., a bipolar sawtooth wave with width equal to 2 ms spreads majority energy within 1000 Hz, and spreads rest of the energy in high-frequency section.

The magnitude of the impulse is related to when and where the impulse is injected, in other words, the injection position and instant. To guarantee the highest SNR without disturbing the stable operation of the system, these three parameters become particularly important in this article.

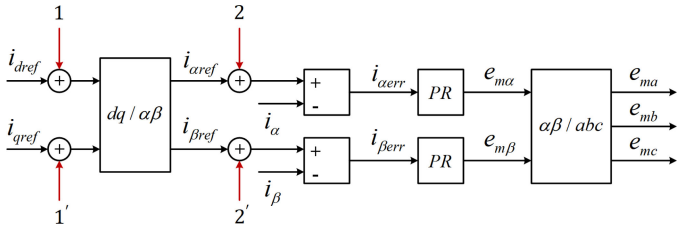

Fig. 16. Generalized current control loop under the stationary reference frame.

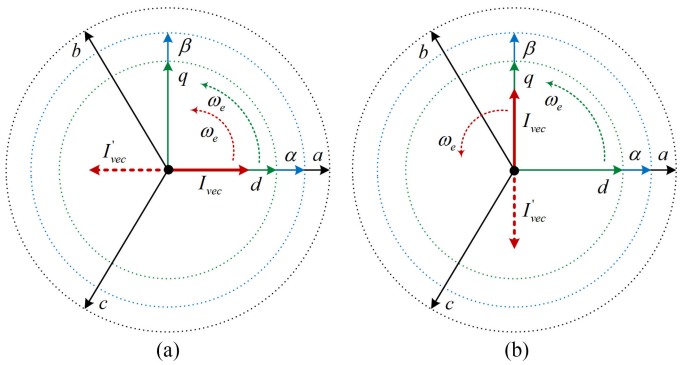

Fig. 17. Spatial position of all three reference frames: dq, $\alpha\beta$, and abc frames. The d-axis overlaps with the α and a axes. The red vector represents the three-phase currents resultant vector, which is rotating counterclockwise in the complex plane with fundamental frequency angular rate ω_e. (a) I_{vec} overlaps with d and α axis. (b) I_{vec} overlaps with q- and β-axis.

A. Control Framework and Its Related Injection Position

In this article, the control loop is implemented under the stationary reference frame. A generalized current control loop is shown in Fig. 16.

The injection position can be chosen as the dq frame or the $\alpha\beta$ frame, which are shown in Fig. 16 as $1(1')$ and $2(2')$, respectively. By mapping the dq, $\alpha\beta$, and abc frames to the complex plane and letting the d-axis overlap with the α- and a-axes, the transformation relationship between different reference frames can be easily obtained (see Fig. 17).

It is noticeable, if the injection position is $1(1')$, namely d- or q-axis, however, that the rotating dq reference frame will distort the impulse waveform in the mapping process. Let $f(t)$ represent the time-domain waveform of the impulse on the d axis, so the impulse under the dq reference frame can be represented by

$$\mathbf{i}_{\mathbf{pdqo}} = \begin{bmatrix} f(t) \\ 0 \\ 0 \end{bmatrix}. \tag{33}$$

Hence, the impulse under the stationary abc reference frame can be calculated by

$$\mathbf{i}_{\mathbf{pabc}} = \mathbf{T}_{\mathbf{dqo/abc}} \cdot \mathbf{i}_{\mathbf{pdqo}} = \begin{bmatrix} \cos(\phi)\, f(t) \\ \cos\left(\phi - \frac{2}{3}\pi\right) f(t) \\ \cos\left(\phi + \frac{2}{3}\pi\right) f(t) \end{bmatrix} \tag{34}$$

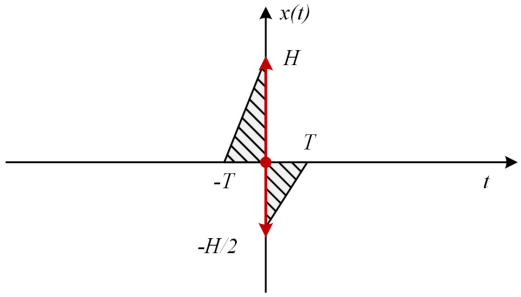

Fig. 18. Idealized impulse for an injected asymmetric bipolar sawtooth wave.

where $\mathbf{T_{dqo/abc}}$, the coordinate transformation matrix mapping from the dq frame to the abc reference frame in constant magnitude form, is usually given by

$$\mathbf{T_{dqo/abc}} = \begin{bmatrix} \cos(\phi) & -\sin(\phi) & \frac{1}{2} \\ \cos\left(\phi - \frac{2}{3}\pi\right) & -\sin\left(\phi - \frac{2}{3}\pi\right) & \frac{1}{2} \\ \cos\left(\phi + \frac{2}{3}\pi\right) & -\sin\left(\phi + \frac{2}{3}\pi\right) & \frac{1}{2} \end{bmatrix} \tag{35}$$

and ϕ is the angle between d and a axes in complex plane.

According to (34), the impulse mapped onto the a axis turns out to be $\cos(\phi)f(t)$, not $f(t)$. When the impulse is injected at the peak point of the current, the value of $\cos(\phi)$ over that short duration is nearly constant, which means that the dq/abc transformation will not obviously distort the waveform at that point. However, only the unipolar wave can be chosen for peak point injection. To use the asymmetric bipolar sawtooth wave in this article, an injection point away from peak point must be chosen. However, when the impulse is injected in another position, especially near the zero-crossing point, where $\phi = (2n+1)\pi/2$ and $n \in Z$, the slope of a cosine function reaches its maximum value, in which case $\cos(\phi)$ cannot be treated as constant. So, in this application, it is better to inject the impulse on the α- or β-axis to avoid this issue.

When the impulse is injected in the $\alpha\beta$ reference frame, the two axes are always stationary in the complex plane, which means the mapping relationship between $\alpha\beta$ and abc is constant without complex operators. Therefore, the impulse spectrum is still aligned with the design purpose.

B. Injection Instant and Its Related Maximum Magnitude

The impulse will be distributed to three phases with different ratios after the $\alpha\beta/abc$ transformation, which may exceed the system rating. To ensure that the currents and voltages always stay in the secure region, the magnitude of the injected impulse is limited. To find the maximum magnitude to guarantee the highest SNR, the optimal injection instant should be identified.

1) Injection Requirements for Current Security: To simplify the analysis, let the injected impulse be an ideal impulse, as shown in Fig. 18.

According to the $\alpha\beta/abc$ transformation, the impulse $f(t)$ will spread to the abc frame with $a:b:c = 1:-\frac{1}{2}:-\frac{1}{2}$. So, the three-phase currents will not exceed the system rating value if and only if

$$\begin{cases} \cos(\phi) + H \le 1 \\ \cos\left(\phi - \frac{2}{3}\pi\right) - \frac{1}{2}H \ge -1 \\ \cos\left(\phi + \frac{2}{3}\pi\right) - \frac{1}{2}H \ge -1 \\ \cos(\phi) - \frac{1}{2}H \ge -1 \\ \cos\left(\phi - \frac{2}{3}\pi\right) + \frac{1}{4}H \le 1 \\ \cos\left(\phi + \frac{2}{3}\pi\right) + \frac{1}{4}H \le 1 \end{cases} \tag{36}$$

where ϕ is the injection phase angle, H is the magnitude of injected impulse. Meanwhile, all the constraint functions have been normalized.

With the same analysis method, when the impulse is injected on the β-axis, the current will stay in the secure region if and only if

$$\begin{cases} \cos\left(\phi - \frac{2}{3}\pi\right) + \frac{\sqrt{3}}{2}H \le 1 \\ \cos\left(\phi + \frac{2}{3}\pi\right) - \frac{\sqrt{3}}{2}H \ge -1 \\ \cos\left(\phi - \frac{2}{3}\pi\right) - \frac{\sqrt{3}}{4}H \ge -1 \\ \cos\left(\phi + \frac{2}{3}\pi\right) + \frac{\sqrt{3}}{4}H \le 1. \end{cases} \tag{37}$$

Equations (36) and (37) are nonlinear programming equation sets, which can be easily calculated computationally. The program structure is summarized in Table IV. The basic idea is to calculate the maximum injection magnitude corresponding to each injection phase angle from 0° to 360°, and compare all these values to get the maximum one.

TABLE IV
PROGRAM STRUCTURE FOR CALCULATING NONLINEAR PROGRAMMING EQUATION SET

Algorithm Program for finding optimal phase angle and magnitude

Procedure Cycle(θ, A)
  AnsMatrix = $[A_0, A_1, A_2, A_3, A_4, A_5]$
  AmpMatrix = zeros()
  for $\phi = 0:360$
    Calculate $\cos(\phi) + A = 1$, **stack** $A_0 \leftarrow A$
    Calculate $\cos\left(\phi - \frac{2}{3}\pi\right) - \frac{1}{2}A = -1$, **stack** $A_1 \leftarrow A$
    Calculate $\cos\left(\phi + \frac{2}{3}\pi\right) - \frac{1}{2}A = -1$, **stack** $A_2 \leftarrow A$
    Calculate $\cos(\phi) - \frac{1}{2}A = -1$, **stack** $A_3 \leftarrow A$
    Calculate $\cos\left(\phi - \frac{2}{3}\pi\right) + \frac{1}{4}A = 1$, **stack** $A_4 \leftarrow A$
    Calculate $\cos\left(\phi + \frac{2}{3}\pi\right) + \frac{1}{4}A = 1$, **stack** $A_5 \leftarrow A$
    AmpMatrix(1,$\phi + 1$) = max(AnsMatrix)
  end for
  OptimalAmp = max(AmpMatrix)
  OptimalAng = find(max(AmpMatrix)) – 1
End procedure

TABLE V
OPTIMAL INJECTION POSITION AND RELATED NORMALIZED MAXIMUM MAGNITUDE UNDER DIFFERENT CONDITIONS

	$\rho = \frac{1}{2}$		$\rho = \frac{1}{3}$	
Axis	Position	Magnitude	Position	Magnitude
α	95°	0.3617	145°	0.5425
β	191°	0.7788	197°	0.8949

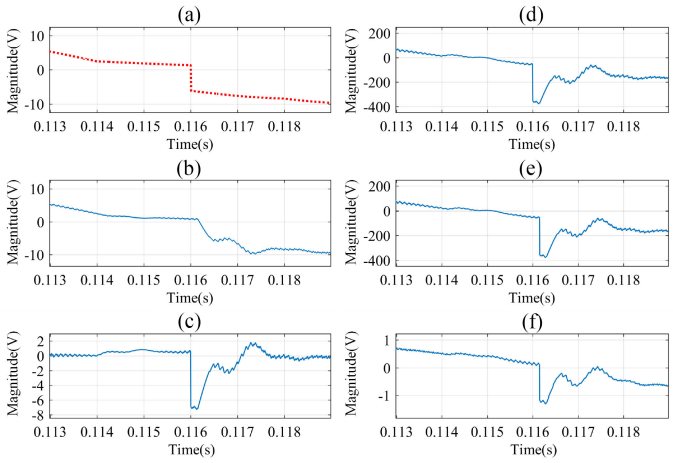

Fig. 19. Simulated waveforms of (a) current reference for the β-axis. (b) Actual current of the β-axis. (c) Error signal. (d) Signal modulated by the PR controller. (e) Signal after the delay. (f) Normalized voltage control signal.

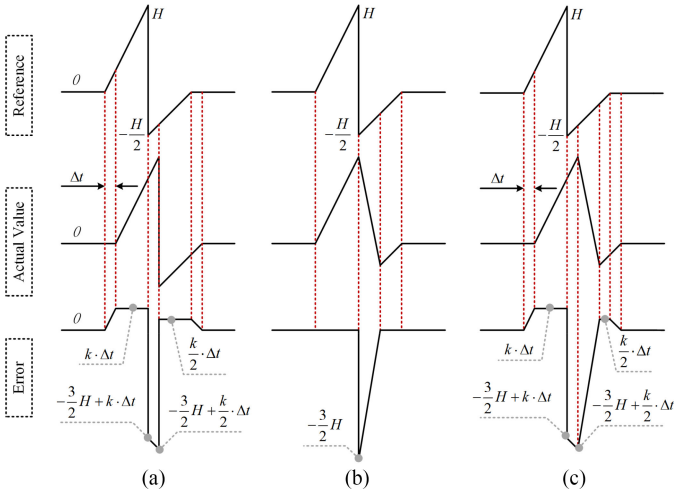

Fig. 20. Influence of system dynamics and delay on an injected asymmetric bipolar sawtooth wave. The first column shows the effect of system delay, the second column illustrates the effect of system dynamic, and the final column combines these two effects. Δt is the system delay, which is equal to 1.5 control cycles in synchronous sampling mode, and k represents the slope of the hypotenuse.

Table V shows the optimal injection instants and their related normalized maximum magnitudes when asymmetric bipolar sawtooth waves are injected with different ρ values on the α- or β-axis. Table V shows that the impulse injected on the β axis can achieve a relative maximum magnitude. The reason behind this phenomenon is that all three phases of the system will be disturbed when injecting an impulse on the α-axis, which has a stricter constraint than injection on the β axis and only phases b and c will be interrupted. In the remainder of this article, we will focus only on the β-axis.

2) Injection Requirements for Voltage Security: The current closed-loop transfer function will affect the injected impulse and cause high-frequency rejection and slight deformation, which is expected in the design. However, in practice, the infinite slope of the impulse will become a major challenge for system dynamic performance and lead to unexpected deformation by overmodulation, which is related to the security and controllability of the voltage.

The basic reasons for overmodulation during impulse injection are insufficient dynamic performance and system delay. The system cannot trace the fast-transient state of the impulse, leading to an inherent error between the reference value of the impulse and its actual value. This phenomenon is exacerbated by system delay. Overmodulation will not significantly affect normal operation of the system because of its short duration, but it will cause unexpected distortion of the impulse, leading to uncontrollable measurement accuracy in the high-frequency section.

The system delay can be clearly observed. During impulse injection, the time positions of the impulse in current and voltage will be delayed by 1.5 control cycles owing to the effect of system delay. Fig. 19 shows this phenomenon.

The system dynamic and delay both influence the injected impulse. Different systems have different dynamic performances, leading to different error signals. Meanwhile, system delay is always equal to 1.5 system control cycles in a synchronous

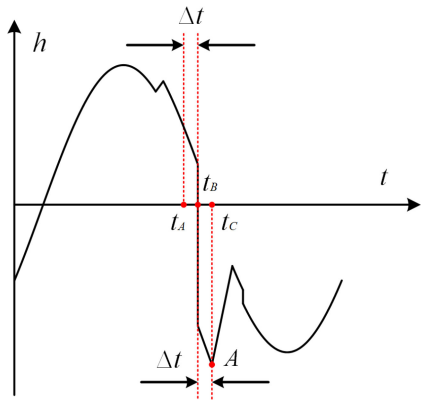

Fig. 21. Waveform of idealized modulation signal of phase b when injecting an asymmetric bipolar sawtooth wave into the system control loop. t_A represents the ideal injection position in the design, t_B represents the actual injection position resulting from system delay, and t_C represents the peak point instant of the modulation signal.

sampling mode. To simplify the analysis of this combined influence, we assume that the signals in the control loop are always ideal, which means that the system has an infinite dynamic performance and traces the reference perfectly. Let the width of an asymmetric bipolar sawtooth wave be 4 ms and the asymmetry ratio be $\rho = 0.5$. Fig. 20 illustrates the analysis results.

The error signals generated in this process will be modulated and amplified by the PR controller and overlaid with the original sinusoidal voltage control signal, leading to possible overmodulation. When the system moves outside its linear region, the PWM generator cannot magnify the voltage control signal perfectly, resulting in deformation of the injected impulse.

For a chosen phase b as the target and an error signal overlaid with a sinusoidal modulation signal, the idealized voltage control signal is shown in Fig. 21.

Let $e_\beta(t)$ represent the error signal. Then the voltage modulation signal will not exceed the linear region of the PWM generator if and only if

$$e_\beta(t)\, G_{\mathrm{PR}} G_{\mathrm{delay}} k_{\beta/b} + \frac{2\sqrt{2}U_{\mathrm{AC}}}{U_{\mathrm{DC}}} \cos\left(\omega t - \frac{2}{3}\pi\right) \geq -M \tag{38}$$

where G_{PR} and G_{delay} represent the transfer function of the PR controller and system delay, respectively, $k_{\beta/b}$ represents the mapping relationship from the β-axis to the b-axis, U_{AC} and U_{DC} are ac-side and dc-side operating voltages, respectively, and M controls the limitation and satisfies $0 < M \leq 1$. In most cases, M can be selected as 0.9 to ensure a high enough injection magnitude and nearly a 10% safety margin.

Obviously, if point A in Fig. 21 does not exceed the linear region, the overall modulation signal will satisfy (38), thus

$$\left(-\frac{3}{2}H + \frac{k}{2}\Delta t\right) G_{\mathrm{PR}} G_{\mathrm{delay}} k_{\beta/b} + \frac{2\sqrt{2}U_{\mathrm{AC}}}{U_{\mathrm{DC}}} \cos\left(\theta_0 + \frac{4\pi\Delta t}{0.02} - \frac{2}{3}\pi\right) \geq -M \tag{39}$$

where θ_0 represents the optimal injection position.

Equation (39) is still complex to use in practice. Therefore, two approximations will be made as follows.

1) The PR controller can be simplified to a proportional amplifier, because k_R will only affect the fundamental frequency component, which can be ignored when analyzing a compound signal.
2) The system delay can be ignored when the switching frequency is high enough.

Hence, (39) can be approximated as follows:

$$-\frac{3}{2}Hk_P k_{\beta/b} + \frac{2\sqrt{2}U_{\mathrm{AC}}}{U_{\mathrm{DC}}} \cos\left(\theta_0 - \frac{2}{3}\pi\right) \geq -M \tag{40}$$

where k_P is a normalized value.

According to Table V, the optimal time position is 191° on the β-axis, thus

$$H \leq \frac{1}{1.3k_P}\left(M + 0.922\frac{U_{\mathrm{AC}}}{U_{\mathrm{DC}}}\right). \tag{41}$$

Meanwhile, the voltage modulation signal of phase c, as shown in Fig. 22, will not exceed the linear region of the PWM generator if and only if

$$e_\beta(t)\, G_{\mathrm{PR}} G_{\mathrm{delay}} k_{\beta/c} + \frac{2\sqrt{2}U_{\mathrm{AC}}}{U_{\mathrm{DC}}} \cos\left(\omega t + \frac{2}{3}\pi\right) \leq M. \tag{42}$$

For the same reason, (42) can be approximated as follows:

$$H \leq \frac{1}{1.3k_P}\left(M - 1.855\frac{U_{\mathrm{AC}}}{U_{\mathrm{DC}}}\right). \tag{43}$$

Equation (43) is more constrained than (41), so the final magnitude of the impulse should be the maximum value constrained by (43) and the optimal injection instant analysis in Table V.

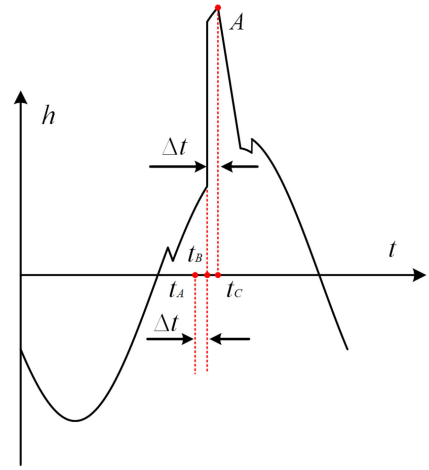

Fig. 22. Waveform of idealized modulation signal of phase c when injecting an asymmetric bipolar sawtooth wave into the system control loop. t_A represents the ideal injection position in the design, t_B represents the actual injection position resulting from system delay, and t_C represents the peak point instant of the modulation signal.

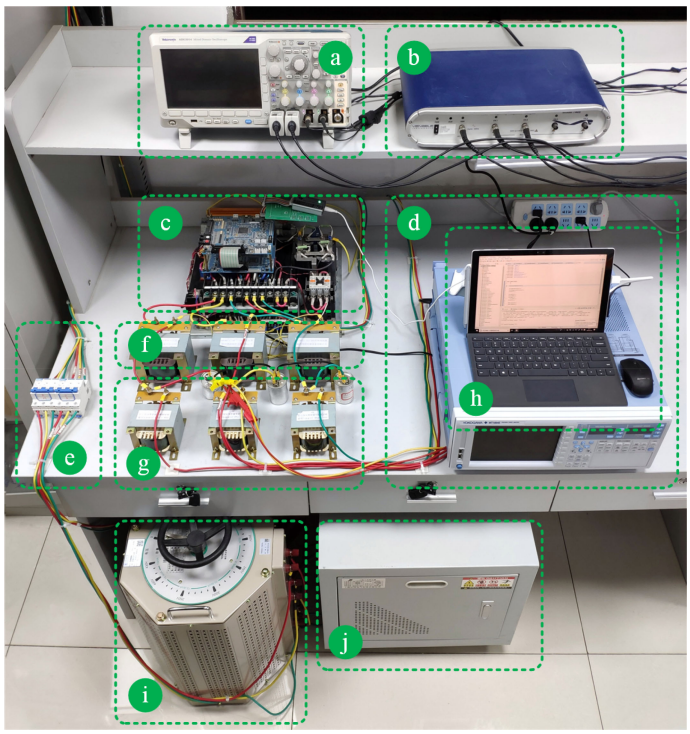

Fig. 23. Photograph of the structure of the experimental prototype. (a) Oscilloscope. (b) Frequency response analyzer. (c) Three-phase VSI. (d) 16-bit power analyzer. (e) DC side switch and grid-connected switch. (f) Output inductor. (g) *LC* filter. (h) PC. (i) Voltage regulator. (j) Isolation transformer.

V. Experimental Implementation and Verification

To verify the reliability of the proposed design method and chosen impulse, an experimental prototype of a three-phase ac DPS is built, as shown in Fig. 23. The system topology and its control method are illustrated in Figs. 2 and 16, and the system parameters are summarized in Table VI. A voltage

TABLE VI
EXPERIMENTAL PROTOTYPE PARAMETERS

Parameter	Value	Parameter	Value
L	3.5 mH	k_P	20
C	15 μF	k_R	3000
L_g	1.75 mH	ω_r	100π
R_g	1 Ω	ω_c	π
T_s	0.1 ms	—	—

regulator and an isolation transformer are used to change the dc side input voltage and realize electrical isolation. A three-phase voltage source inverter (VSI), which is controlled as a current source, is employed to perform the dc to ac transformation, and the switching frequency harmonics in the output current are reduced by the output inductor. An *LC* filter is introduced as part of the system grid impedance, where a resistor with low resistance is also connected in series. The ideal power grid is implemented by using a regenerator grid simulator. The high-vertical-resolution sampling is accomplished by using a 16-bit power analyzer and monitoring of three-phase variables is done with an 8-bit oscilloscope. To get the actual reference value of the grid impedance instead of using the theoretical value, a traditional sweep method is also adopted in this article by using a frequency response analyzer and employing a high-accuracy sweep method.

A. Experimental Implementation

1) Hardware Setup and Digital Implementation: During the design procedure, the optimal injection position and instant and its related maximum injection magnitude can be calculated based on (43) and Table V. The system is operated in grid-tied mode, with $V_{\rm DC} = 450$ V, $v_{\rm AC} = 110$ V, and $I_d = 10$ A. Other parameters are summarized in Table VI.

Let $M = 1$, and then the calculated maximum injection magnitude is 4.7 with the chosen system parameters. However, to maintain a certain safety margin, only 90% of the calculated magnitude (4.2) is taken. The optimal injection instant is 191° on the β-axis according to Table V. To enhance the injection power, the width of the impulse is designed as 0.004 s, which is $1/5$ of the system cycle.

The PLL angle is the core of the injection process. When the output angle of PLL equals to the designed optimal angle, θ^*, the DSP will start to add the impulse to the original reference. The output angle also controls the sampling instant of power analyzer, i.e., when $\theta = 0$, the analyzer will start to record for one or more cycles. The data processing is complete by a PC. It can also be embedded in the DSP to realize real-time calculation [31], but it is out of the scope of this article. The digital implementation of injection, control and data processing is shown in Fig. 24.

The reference value of grid impedance is obtained by using the traditional sweep method. In this article, the grid impedance includes the *LC* filter and a series resistor R_g. The sweep method is only applied to this circuit, without measuring the cable and the grid simulator.

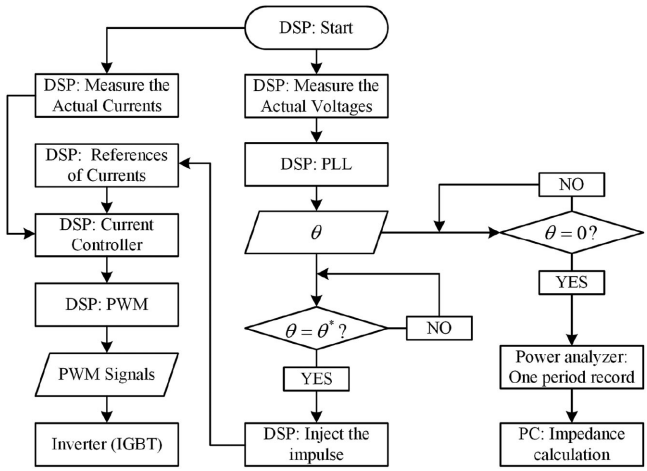

Fig. 24. Digital implementation of injection, control, and data processing.

2) Practical Issues in Data Processing: The common data processing method can be referred to Section II. However, there are two main practical issues that exist in calculation.

First, steady-state compensation is somewhat sensitive to asynchronized data sequences, which suffers from frequency fluctuation, magnitude change, and phase deviation. Take the fundamental frequency fluctuation as an example, thus

$$\cos(\omega_e t) - \cos(\omega_e' t) = -2\sin\left(\frac{\omega_e t + \omega_e' t}{2}\right)\sin\left(\frac{\omega_e t - \omega_e' t}{2}\right) \tag{44}$$

where ω_e and ω_e' are ideal and actual fundamental frequency, respectively. This error signal is not caused by the perturbation but is generated by fluctuations, which turns out to be a random error without reflecting any impedance characteristics.

If the system is completely stable, i.e., the frequency is fully controlled by the inverter in islanding mode, the data synchronization is easy to implementation where only one cycle data sequence is needed. However, the system is not always well controlled. The errors caused by unsynchronized data are random errors which can be eliminated by average method. If the computation burden is not considered, the nonlinear average method can also be applied to gain a higher accuracy [43].

Second, when applying the impulse injection method to a high-speed measurement scenario, because of the time limitation, only a few cycles of data can be measured and thus the FFT calculation will have a relatively low-frequency resolution. The zero-padding method is utilized to generate a long zero-data sequence in this article. In the compensated data sequence, except for the impulse part, the rest of the sequence should be zero, but it still includes noise from the imperfect compensation. Therefore, when applying the zero-padding method to extend the data length, one can replace the original nonzero part except for the cycle with the impulse. The process is illustrated in Fig. 25. The zero-padding method helps to eliminate noise in the compensated data and improve frequency resolution.

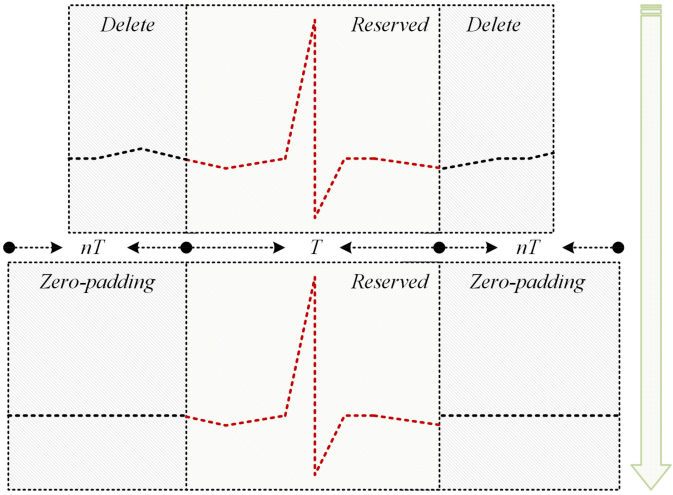

Fig. 25. Original waveform (top) and waveform processed by zero-padding method (bottom). n is decided by required frequency resolution, and the resolution is the reciprocal of the time length of the data sequence.

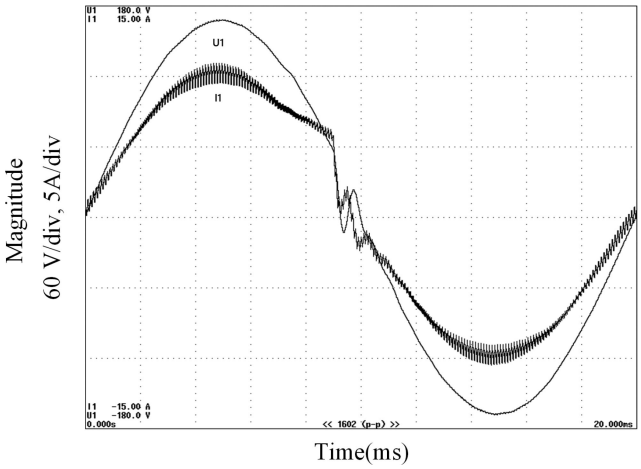

Fig. 26. Experimental waveforms of current and voltage captured by a 16-bit power analyzer when injecting an asymmetric bipolar sawtooth wave on the β axis at 191°. Only phase b is measured to get the single-phase impedance.

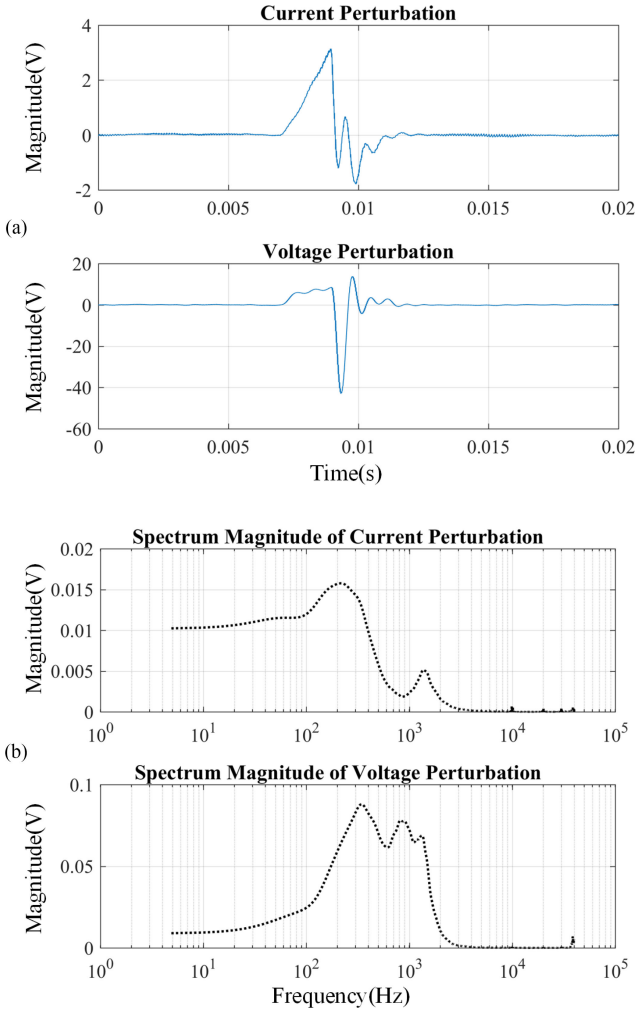

Fig. 27. (a) Actual injected impulse waveform obtained with steady-state compensation after averaging 20 times. (b) Spectrum of the injected impulse of phase b when injecting an asymmetric bipolar sawtooth wave on the β axis at 191°.

B. Demonstration of Selected Impulse and Design

With the data captured by the 16-bit power analyzer, as shown in Fig. 26, the actual injection impulse can be obtained by steady-state compensation. The designed impulse will be affected by the system closed loop, whereby the actual impulse is different from the ideal one. This phenomenon has been considered in the design procedure. Fig. 27(a) illustrates this phenomenon, and Fig. 27(b) shows the related impulse spectrum, where the distribution characteristics are as expected.

An 8-bit oscilloscope is used to monitor the three-phase currents and voltages. As shown in Fig. 28, with the designed impulse, the currents and voltages will always stay in the safety region and will not exceed the system rating. The system is free from being severely disturbed. It can also be observed that phase a is nearly not disturbed, which can significantly reduce the total harmonic distortion of the three-phase variables when the impulse is injected.

Fig. 29 shows the calculated grid impedance averaged over 20 samples. The transfer function estimation method, which has shown a higher accuracy than the FFT because of its correlation processing, is also employed when calculating the impedance. The slight difference around 900 Hz between the reference and the measured value is because the reference value does not incorporate the impedance of the cable and the grid simulator, while the measured value includes the entire impedance of the system side. For this reason, the error can be considered as acceptable and the measured value is nearly equal to the reference up to 5000 Hz, or $1/2$ of the system switching frequency in this article.

A simple comparison is also implemented to identify the effectiveness of the averaging method with different sampling cycles. Fig. 30 illustrates the results. With averaging over 1, 5, 10, and 15 samples, the background noise existing in the steady-state signals have been extracted with a decreasing magnitude. Fig. 31 presents the corresponding calculation results with increasing accuracy. Fig. 31 also demonstrates that the accuracy of averaging over five samples is high enough.

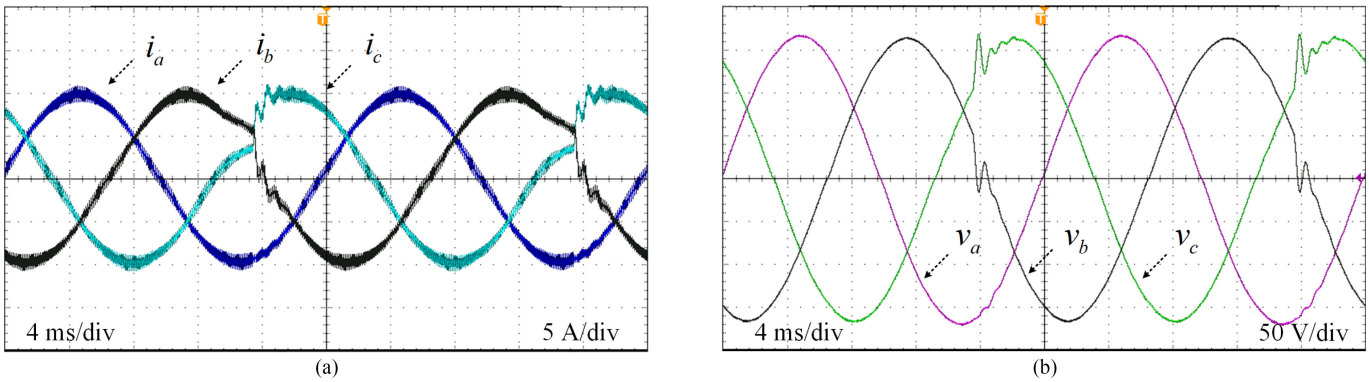

Fig. 28. Waveforms of (a) three-phase currents and (b) three-phase voltages when injecting a well-designed asymmetric bipolar sawtooth wave.

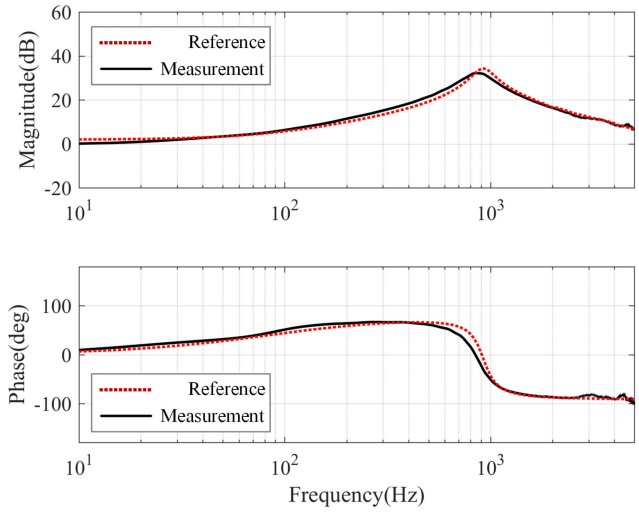

Fig. 29. Bode plot of calculated grid impedance with 20 times averaging when injecting a well-designed asymmetric bipolar sawtooth wave.

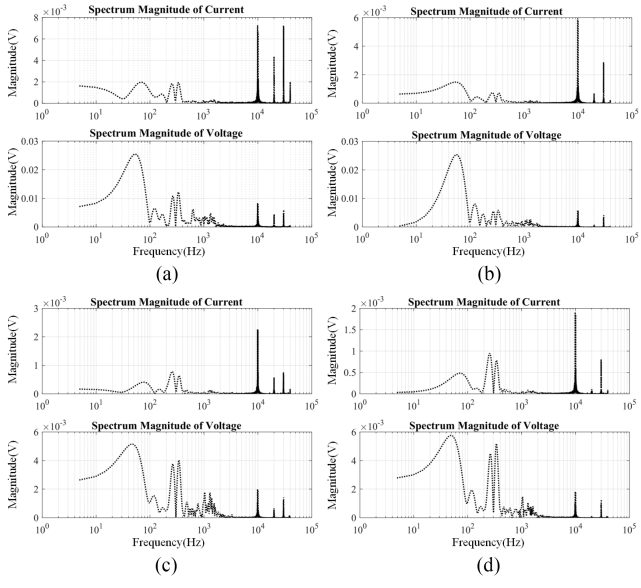

Fig. 30. Background noise with different average number of samples. (a) Single sample. (b) Average over 5 samples. (c) Average over 10 samples. (d) Average over 15 samples.

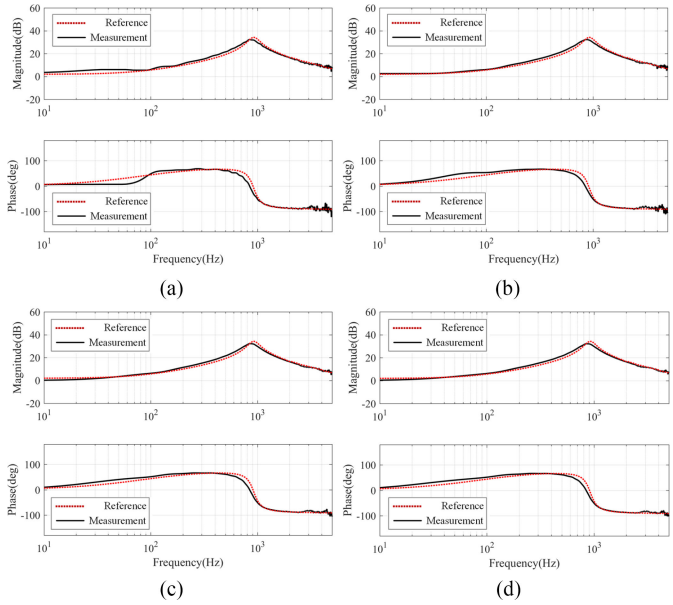

Fig. 31. Bode plot of measured grid impedance with different average number of samples when injecting an asymmetric bipolar sawtooth wave. (a) Single sample. (b) Average over 5 samples. (c) Average over 10 samples. (d) Average over 15 samples.

However, to compare different impulses with a higher accuracy to show the fundamental properties, this article will always average over 20 samples for all types of impulses. In practice or in field tests, five samples averaging is totally enough according to the analysis, especially when nonlinear average method is applied.

C. *Comparison to Existing Impulse Injection Method*

In existing impulse injection methods, unipolar triangular waves and symmetric bipolar waves have been used with specific injection instants. In impulse analysis, unipolar impulses are unsuitable for broadband measurement owing to their high-energy distribution in the low-frequency band, especially for triangular or square waves, which have zero-magnitude points in their spectra. For bipolar impulse, the FFT analysis shows that the symmetric bipolar impulse cannot be used for measuring the

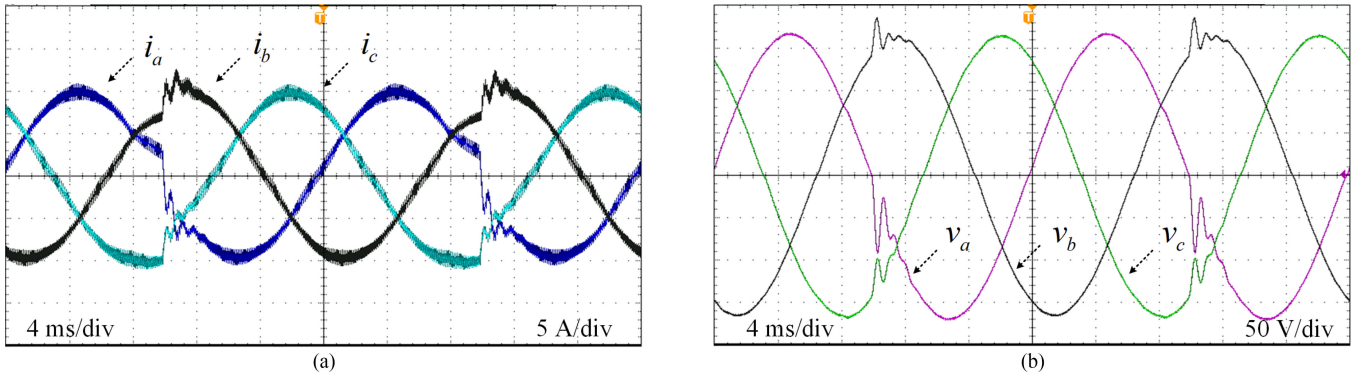

Fig. 32. Waveforms of (a) three-phase currents and (b) three-phase voltages when injecting a symmetric bipolar sawtooth wave.

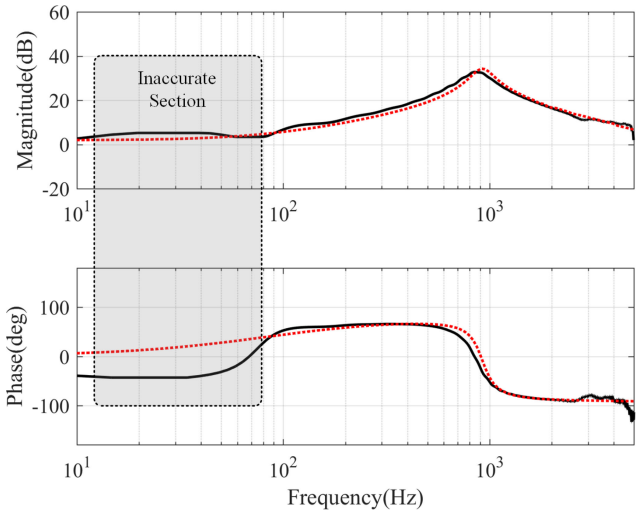

Fig. 33. Bode plot of calculated grid impedance with 20 times averaging when injecting a symmetric bipolar sawtooth wave at the zero-crossing point.

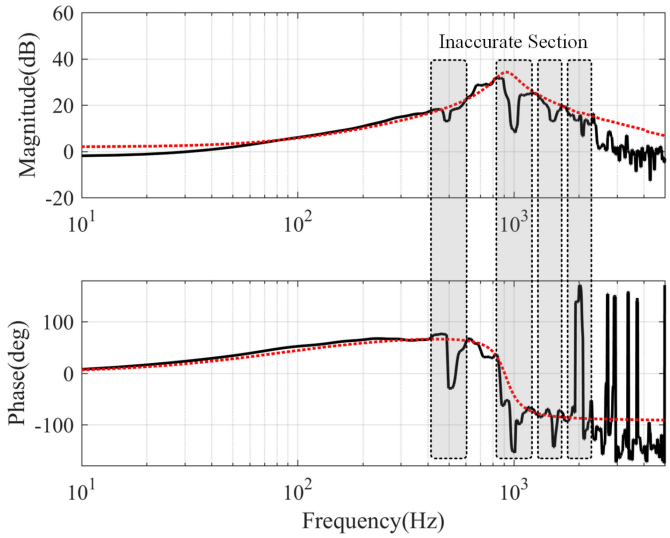

Fig. 34. Bode plot of calculated grid impedance with 20 times averaging when injecting a unipolar triangular wave at the peak point.

low-frequency band. To verify these characteristics, two sets of experiments have been implemented with the same system parameters.

1) Measurement With a Symmetric Bipolar Sawtooth Wave: In this case, the system is controlled with the same parameters as Table VI shows. A symmetric bipolar sawtooth wave, injecting on the α-axis at the zero-crossing point of phase a, is designed with the same magnitude and width as in the former experiment to achieve a fair comparison, where the magnitude is 4.2 and width is 0.004 s.

Injecting a symmetric bipolar impulse at the zero-crossing point can easily cause the current and voltage to exceed the system steady-state operating values when the magnitude of impulse is free from design. Traditionally, the magnitude is set as 1.0 to 1.5 per unit (p.u.), or even higher. In this article, the magnitude is only 4.2, or 0.42 p.u., but it still has a higher transient response than that of the asymmetric impulse. Fig. 32 shows the three-phase variables when injecting a symmetric bipolar sawtooth wave.

Fig. 33 shows the results. It can be observed that the accuracy in the low-frequency band, especially below 100 Hz, is significantly lower than that for the asymmetric impulse. The fundamental reason for this is that the spectrum distribution of the symmetric bipolar wave does not meet the measurement requirements in practice, which should be avoided.

2) Measurement With a Unipolar Triangular Wave: In this case, the system parameters and the injected impulse are also consistent with those in previous experiments. To ensure that the currents and voltages will not heavily exceed the system rating during impulse injection, the traditional unipolar injection method is to apply the injection at the peak point of the current, which will also be adopted in this article.

The magnitude of the impulse is set to 4.2, and the width is 0.004 s to achieve a fair comparison. Fig. 34 shows the results. The inaccurate sections are equally spaced at 500 Hz because of the distribution of zero-magnitude points in its spectrum. It is true that the accuracy is limited by the impulse properties. However, when the slope of the triangular wave is higher than a certain value, the spectrum property is remarkably similar to an ideal sawtooth wave. In addition, Fig. 35 illustrates the monitoring results. It is noticeable, in this article, the magnitude of unipolar triangular wave is only 0.42 p.u., which is very low compared to traditional method where 1.0 p.u. or even larger magnitude will be adopted.

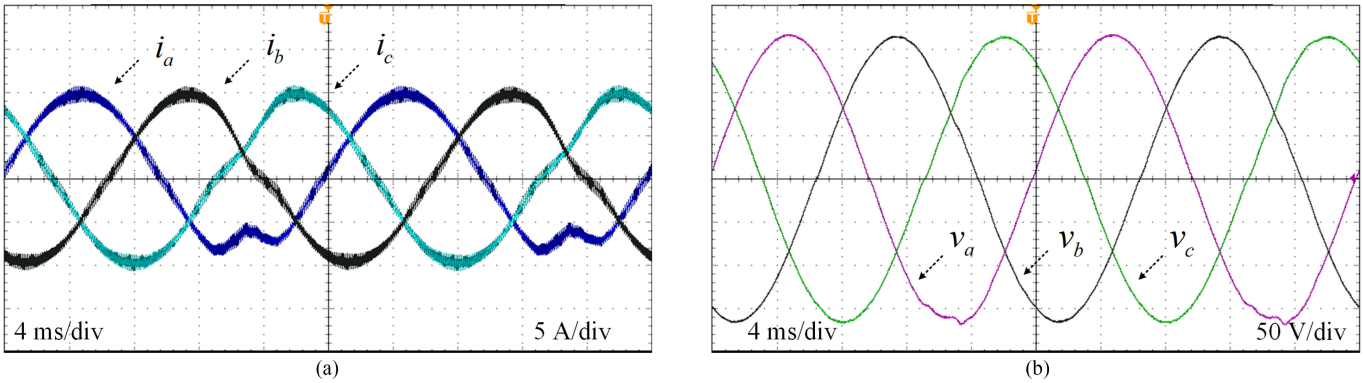

Fig. 35. Waveforms of (a) three-phase currents and (b) three-phase voltages when injecting a unipolar triangular wave.

VI. Conclusion

Applications of grid impedance in stability assessment of grid-tied inverter systems make high-speed and accurate grid impedance measurement methods increasingly important, and the impulse injection method applied under control loop without external perturbation injectors is widely employed. This article proposes a systematic guidance for impulse analysis and design to get rid of the existing issues in impulse-injection-based grid impedance identification method. By assembling a spectrum comparison of several basic impulses with unipolar and bipolar forms and analyzing the impulse parameter characteristics with the Fourier transformation, an impulse selection guidance for different measurement scenarios has been proposed. A parameter design method based on the optimal injection position and instant is also proposed to reduce system burden and guarantee accuracy in broadband measurement.

The traditional unipolar triangular wave and symmetric bipolar sawtooth wave has been chosen as the control group in the experiment. Compared to traditional methods, the well-designed asymmetric bipolar sawtooth wave, injected at 191° on the β axis, exhibits higher reliability and accuracy in broadband measurement and lower burden to the system. It can also be applied to standalone systems.

References

[1] J. Sun, "Impedance-based stability criterion for grid-connected inverters," *IEEE Trans. Power Electron.*, vol. 26, no. 11, pp. 3075–3078, Nov. 2011.

[2] R. D. Middlebrook, "Input filter consideration in design and application of switching regulators," in *Proc. IEEE Ind. Appl. Soc. Annu. Meeting*, 1976, pp. 366–382.

[3] J. Liu, X. Feng, F. C. Lee, and D. Borojevich, "Stability margin monitoring for DC distributed power systems via perturbation approaches," *IEEE Trans. Power Electron.*, vol. 18, no. 6, pp. 1254–1261, Nov. 2003.

[4] A. Riccobono and E. Santi, "Comprehensive review of stability criteria for DC power distribution systems," *IEEE Trans. Ind. Appl.*, vol. 50, no. 5, pp. 3525–3535, Sep./Oct. 2014.

[5] M. Belkhayat, "Stability criterion for AC power systems with regulated loads," Ph.D. dissertation, Dept. Elect. Comput. Eng., Purdue Univ., West Lafayette, IN, USA, 1997.

[6] Z. Liu, J. Liu, W. Bao, and Y. Zhao, "Infinity-norm of impedance-based stability criterion for three-phase AC distributed power systems with constant power loads," *IEEE Trans. Power Electron.*, vol. 30, no. 6, pp. 3030–3043, Jun. 2015.

[7] M. Jaksic, Z. Shen, I. Cvetkovic, D. Boroyevich, R. Burgos, and P. Mattavelli, "Multi-level single-phase shunt current injection converter used in small-signal dq impedance identification," in *Proc. IEEE Appl. Power Electron. Conf. Expo.*, 2014, pp. 2775–2782.

[8] Z. Shen, M. Jaksic, P. Mattavelli, D. Boroyevich, J. Verhulst, and M. Belkhayat, "Design and implementation of three-phase AC impedance measurement unit (IMU) with series and shunt injection," in *Proc. 28th Annu. IEEE Appl. Power Electron. Conf. Expo.*, 2013, pp. 2674–2681.

[9] G. Francis, R. Burgos, D. Boroyevich, F. Wang, and K. Karimi, "An algorithm and implementation system for measuring impedance in the D-Q domain," in *Proc. IEEE Energy Convers. Congr. Expo.*, 2011, pp. 3221–3228.

[10] J. Huang, K. A. Corzine, and M. Belkhayat, "Small-signal impedance measurement of power-electronics-based AC power systems using line-to-line current injection," *IEEE Trans. Power Electron.*, vol. 24, no. 2, pp. 445–455, Feb. 2009.

[11] Z. Liu, I. Cvetkovic, Z. Shen, D. Boroyevich, R. Burgos, and J. Liu, "Imbalance mechanism and balancing control of DC voltages in a transformerless series injector based on paralleled h-bridge converters for AC impedance measurement," *IEEE Trans. Power Electron.*, vol. 34, no. 8, pp. 8175–8189, Aug. 2019.

[12] X. Yue, Z. Fang, F. Wang, Z. Zhang, and H. Shi, "A novel adaptive frequency injection method for power electronic system impedance measurement," *IEEE Trans. Power Electron.*, vol. 29, no. 12, pp. 6700–6711, Dec. 2014.

[13] B. Zhou *et al.*, "Small-signal impedance identification of three-phase diode rectifier with multi-tone injection," in *Proc. IEEE Appl. Power Electron. Conf. Expo.*, 2014, pp. 2746–2753.

[14] T. Roinila, M. Vilkko, and T. Suntio, "Fast loop gain measurement of a switched-mode converter using a binary signal with a specified fourier amplitude spectrum," *IEEE Trans. Power Electron.*, vol. 24, no. 12, pp. 2746–2755, Dec. 2009.

[15] V. Valdivia, A. Lázaro, A. Barrado, P. Zumel, C. Fernández, and M. Sanz, "Impedance identification procedure of three-phase balanced voltage source inverters based on transient response measurements," *IEEE Trans. Power Electron.*, vol. 26, no. 12, pp. 3810–3816, Dec. 2011.

[16] M. Sumner, B. Palethorpe, D. W. P. Thomas, P. Zanchetta, and M. C. Di Piazza, "A technique for power supply harmonic impedance estimation using a controlled voltage disturbance," *IEEE Trans. Power Electron.*, vol. 17, no. 2, pp. 207–215, Mar. 2002.

[17] T. Roinila, H. Abdollahi, S. Arrua, and E. Santi, "Real-time stability analysis and control of multiconverter systems by using MIMO-identification techniques," *IEEE Trans. Power Electron.*, vol. 34, no. 4, pp. 3948–3957, Apr. 2019.

[18] A. Riccobono, M. Mirz, and A. Monti, "Noninvasive online parametric identification of three-phase AC power impedances to assess the stability of grid-tied power electronic inverters in LV networks," *IEEE J. Emerg. Sel. Topics Power Electron.*, vol. 6, no. 2, pp. 629–647, Jun. 2018.

[19] M. Sumner, B. Palethorpe, and D. W. P. Thomas, "Impedance measurement for improved power quality-Part 1: the measurement technique," *IEEE Trans. Power Del.*, vol. 19, no. 3, pp. 1442–1448, Jul. 2004.

[20] T. Roinila, M. Vilkko, and J. Sun, "Broadband methods for online grid impedance measurement," in *Proc. IEEE Energy Convers. Congr. Expo.*, 2013, pp. 3003–3010.

[21] G. B. Stan, J. J. Embrechts, and D. Archambeau, "Comparison of different impulse response measurement techniques," *J. Audio Eng. Soc.*, vol. 50, pp. 249–262, 2002.
[22] L. Ljung, *System Identification: Theory for the User*. Upper Saddle River, NJ, USA: Prentice-Hall, 1999.
[23] B. Miao, R. Zane, and D. Maksimovic, "System identification of power converters with digital control through cross-correlation methods," *IEEE Trans. Power Electron.*, vol. 20, no. 5, pp. 1093–1099, Sep. 2005.
[24] M. Nagpal, W. Xu, and J. Sawada, "Harmonic impedance measurement using three-phase transients," *IEEE Trans. Power Del.*, vol. 13, no. 1, pp. 272–277, Jan. 1998.
[25] M. J. Bridgeman, R. E. Morrison, and S. B. Tenakoon, "Measurement of harmonic impedance on an LV system utilising power capacitor switching and consequent predictions of capacitor induced harmonic distortion," in *Proc. 8th Int. Conf. Harmonics Qual. Power*, 1998, vol. 2, pp. 1141–1145.
[26] L. S. Czarnecki and Z. Staroszczyk, "On-line measurement of equivalent parameters for harmonic frequencies of a power distribution system and load," *IEEE Trans. Instrum. Meas.*, vol. 45, no. 2, pp. 467–472, Apr. 1996.
[27] M. Ciobotaru, R. Teodorescu, P. Rodriguez, A. Timbus, and F. Blaabjerg, "Online grid impedance estimation for single-phase grid-connected systems using PQ variations," in *Proc. IEEE Power Electron. Spec. Conf.*, 2007, pp. 2306–2312.
[28] A. V. Timbus, R. Teodorescu, and P. Rodriguez, "Grid impedance identification based on active power variations and grid voltage control," in *Proc. IEEE Ind. Appl. Annu. Meeting*, 2007, pp. 949–954.
[29] Q. Dou, J. Liu, Z. Liu, and T. Liu, "A novel online grid impedance measurement method based on injecting pulses designed in frequency-domain," in *Proc. IEEE 8th Int. Power Electron. Motion Control Conf.*, 2016, pp. 2931–2936.
[30] Q. Dou, Z. Liu, J. Liu, and W. Bao, "A novel impedance measurement method for three-phase power electronic systems," in *Proc. 9th Int. Conf. Power Electron. ECCE Asia*, 2015, pp. 2282–2287.
[31] M. Céspedes and J. Sun, "Online grid impedance identification for adaptive control of grid-connected inverters," in *Proc. IEEE Energy Convers. Congr. Expo.*, 2012, pp. 914–921.
[32] Z. Liu, J. Liu, Z. Liu, T. Liu, and Y. Tu, "The optimization analysis of impulse injection method for impedance measurement in three-phase power electronic systems," in *Proc. IEEE 3rd Int. Future Energy Electron. Conf. Asia*, 2017, pp. 1623–1627
[33] B. Palethorpe, M. Sumner, and D. W. P. Thomas, "Power system impedance measurement using a power electronic converter," in *Proc. 9th Int. Conf. Harmonics Qual. Power. Proc.*, 2000, vol. 1, pp. 208–213.
[34] P. García, M. Sumner, Á. Navarro-Rodríguez, J. M. Guerrero, and J. García, "Observer-based pulsed signal injection for grid impedance estimation in three-phase systems," *IEEE Trans. Ind. Electron.*, vol. 65, no. 10, pp. 7888–7899, Oct. 2018.
[35] H. L. M. Monteiro *et al.*, "Harmonic impedance measurement based on short time current injections," *Elect. Power Syst. Res.*, vol. 148, pp. 108–116, Jul. 2017.
[36] M. Cespedes and J. Sun, "Adaptive control of grid-connected inverters based on online grid impedance measurements," *IEEE Trans. Sustain. Energy*, vol. 5, no. 2, pp. 516–523, Apr. 2014.
[37] J. Schoukens, R. Pintelon, E. Van Der Ouderaa, and J. Renneboog, "Survey of excitation signals for FFT based signal analyzers," *IEEE Trans. Instrum. Meas.*, vol. 37, no. 3, pp. 342–352, Sep. 1988.
[38] Z. Staroszczyk, "A method for real-time, wide-band identification of the source impedance in power systems," *IEEE Trans. Instrum. Meas.*, vol. 54, no. 1, pp. 377–385, Feb. 2005.
[39] L. Asiminoaei, R. Teodorescu, F. Blaabjerg, and U. Borup, "Implementation and test of an online embedded grid impedance estimation technique for PV inverters," *IEEE Trans. Ind. Electron.*, vol. 52, no. 4, pp. 1136–1144, Aug. 2005.
[40] B. Wen, D. Boroyevich, R. Burgos, P. Mattavelli, and Z. Shen, "Analysis of D-Q small-signal impedance of grid-tied inverters," *IEEE Trans. Power Electron.*, vol. 31, no. 1, pp. 675–687, Jan. 2016.
[41] M. Parvez, M. F. M. Elias, and N. A. Rahim, "Performance analysis of PR current controller for single-phase inverters," in *Proc. 4th IET Clean Energy Technol. Conf.*, 2016, pp. 1–8.
[42] T. Liu, Z. Liu, J. Liu, Y. Tu, and Z. Liu, "Stability enhancement of single-loop inverter-side current feedback controlled grid-connected inverters with LCL filters," in *Proc. IEEE Energy Convers. Congr. Expo.*, 2017, pp. 3030–3037.
[43] P. Guillaume, "Frequency response measurements of multivariable systems using nonlinear averaging techniques," *IEEE Trans. Instrum. Meas.*, vol. 47, no. 3, pp. 796–800, Jun. 1998.

Zipeng Liu (Student Member, IEEE) received the B.S. degree in electrical engineering and automation from Sichuan University, Sichuan, China, in 2015. He is currently working toward the Ph.D. degree with Xi'an Jiaotong University, Xi'an, China.

His research interests include impedance measurement and stability analysis of three-phase ac power electronics systems.

Jinjun Liu (Fellow, IEEE) received the B.S. and Ph.D. degrees in electrical engineering from Xi'an Jiaotong University (XJTU), Xi'an, China, in 1992 and 1997, respectively.

He then joined the XJTU Electrical Engineering School, as a Faculty. From late 1999 to early 2002, he was with the Center for Power Electronics Systems, Virginia Polytechnic Institute and State University, Blacksburg, VA, USA, as a Visiting Scholar. In late 2002, he was promoted to a Full Professor and then the Head of the Power Electronics and Renewable Energy Center, XJTU, which now comprises 21 faculty members and over 150 graduate students and carries one of the leading power electronics programs in China. From 2005 to early 2010, he served as an Associate Dean of Electrical Engineering School, XJTU, and from 2009 to early 2015, the Dean for Undergraduate Education of XJTU. He is currently an XJTU Distinguished Professor of power electronics. He has coauthored three books (including one textbook), published more than 400 technical papers in peer-reviewed journals and conference proceedings, holds over 50 invention patents (China/U.S.), and delivered for many times plenary keynote speeches and tutorials at IEEE conferences or China national conferences in power electronics area. His research interests include modeling, control, and design methods for power converters and electronified power systems, power quality control and utility applications of power electronics, and microgrids for sustainable energy and distributed generation.

Dr. Liu received was the recipient of governmental awards eight times at national level or provincial/ministerial level for scientific research/teaching achievements. He was also the recipient of the 2006 Delta Scholar Award, the 2014 Chang Jiang Scholar Award, the 2014 Outstanding Sci-Tech Worker of the Nation Award, and the IEEE Transactions on Power Electronics 2016 Prize Paper Award. He served as the IEEE Power Electronics Society Region 10 Liaison and then China Liaison for 10 years, an Associate Editor for the IEEE TRANSACTIONS ON POWER ELECTRONICS for 13 years, the Executive Vice President from 2015 to 2019, and the Vice President for duration 2020–2021 for membership of IEEE PELS. He is on the Board of China Electrotechnical Society, and was elected the Vice President in 2013 and the Secretary General in 2018 at the CES Power Electronics Society. Since 2013, he has been the Vice President for International Affairs, China Power Supply Society (CPSS), and since 2016, the inaugural Editor-in-Chief of *CPSS Transactions on Power Electronics and Applications*. Since 2013, he has been serving as the Vice Chair of the Chinese National Steering Committee for College Electric Power Engineering Programs.

Zeng Liu (Member, IEEE) received the B.S. degree from Hunan University, Changsha, China, in 2006, and the M.S. and Ph.D. degrees from Xi'an Jiaotong University (XJTU), Xi'an, China, in 2009 and 2013, respectively, all in electrical engineering.

He then joine as a Faculty Member in electrical engineering, XJTU, where he is currently an Associate Professor. From 2015 to 2017, he was with the Center for Power Electronics Systems, Virginia Polytechnic Institute and State University, Blacksburg, VA, USA, as a Visiting Scholar. His research interests include control of power systems with multiple converters for renewable energy and energy storage applications, and small-signal stability of power electronics systems.

Dr. Liu was the recipient of an IEEE TRANSACTIONS ON POWER ELECTRONICS Prize Paper Award in 2016, and served as Secretary-General for *2019 IEEE 10th International Symposium on Power Electronics for Distributed Generation Systems*.